SILICON MATERIALS TASK OF THE LOW COST SOLAR ARRAY PROJECT (PART 2)

Research Report 76-904-SIMAT-R1

FIRST QUARTERLY REPORT

1 October 1975 - 31 December 1975

R. H. Hopkins, J. R. Davis,
P. Rai-Choudhury, and P. D. Blais

and

J. R. McCormick
Dow Corning Corporation

February 20, 1976

Contract No. 954331

This work was performed for the Jet Propulsion Laboratory, California Institute of Technology, sponsored by the National Aeronautics and Space Administration under Contract NAS 7-100.

SILICON MATERIALS TASK OF THE LOW COST SOLAR ARRAY PROJECT (PART 2)

Research Report 76-9C4-SIMAT-R1

FIRST QUARTERLY REPORT

1 October 1975 - 31 December 1975

R. H. Hopkins, J. R. Davis,
P. Rai-Choudhury, and P. D. Blais

and

J. R. McCormick
Dow Corning Corporation

February 20, 1976

Contract No. 954331

This work was performed for the Jet Propulsion Laboratory, California Institute of Technology, sponsored by the National Aeronautics and Space Administration under Contract NAS 7-100.

CONTENTS

CONTENTS (Con't)

FIGURE CAPTIONS

LIST OF TABLES

FIRST QUARTERLY REPORT

1 October 1975 - 31 December 1975
Contract No. 954331

SILICON MATERIALS TASK

1. SUMMARY

The objective of this program, Part 2 of the Silicon Materials Task, is to develop and define purity requirements for solar cell grade (SG) silicon material by evaluating the effects of specific impurities and impurity levels on the performance of silicon solar cells. A secondary goal is to generate data which forms the basis for cost-tradeoff analyses of silicon solar cell material. This portion of the program is being carried out by a team of scientists at the Westinghouse Research Labs and Dow Corning Corporation.

The basic approach of the program is to establish, as unambiguously as possible, what concentrations of the impurities commonly found in silicon starting material (metallurgical grade silicon) can be tolerated in silicon crystals produced by both the standard Czochralski and the dendritic-web sheet (rapid growth) methods without degrading solar cell performance. The tolerable impurity levels will be bracketed by iterating impurity concentrations over several generations of silicon crystals. The crystal impurity concentration range for the first generation, about 10^{15} cm^{-3}, was chosen at a level where incipient effects on solar cell performance should occur and where reliable mass spectroscopy can be performed for chemical analysis. Impurity levels will be adjusted up or down in subsequent generations. All crystals contain a baseline boron doping (2-6 Ωcm).

Each ingot and wafer will be subjected to a battery of tests to evaluate its chemistry, microstructure, electrical properties and solar cell performance in order to define Solar Grade material. The techniques employed for bulk and wafer analysis include, e.g., optical and x-ray microscopy, mass spectroscopy, neutron activation analysis, lifetime measurements, diode and solar cell parameter measurements.

The program is on schedule in all elements. Specifically, the growth, evaluation, solar cell fabrication and testing is completed for the baseline boron-doped Czochralski material. Cell efficiencies are in the 11-13% range (AM1). The growth of six first generation Czochralski crystals (boron doping plus Cr, Mn, Cu, Ni, V, and Ti) is completed. Solar cell measurements on four of the first doubly-doped ingots indicates that Cr and Mn seriously degrade cell performance at the 10^{15} cm^{-3} doping level while neither Ni nor Cu produce any significant reduction in cell efficiency. The results for Ni can be rationalized on the basis of its known gettering properties. The results for Cu are surprising and may indicate that precipitation of Cu or gettering during diffusion have rendered it inactive as a recombination center.

2. INTRODUCTION

2.1 Program Objective

The objective of this program, Part 2 of the Silicon Materials Task, is to develop and define purity requirements for solar cell grade (SG) silicon material by evaluating the effects of specific impurities and impurity levels on the performance of silicon solar cells. A secondary goal is to generate data which forms the basis for cost-tradeoff analyses of silicon solar cell material.

2.2 Program Approach

The basic approach we have taken is to establish, as unambiguously as possible, what concentrations of the impurities commonly found in silicon starting material (metallurgical grade silicon) can be tolerated in silicon wafers produced by (a) standard Czochralski pulling and (b) rapid sheet growth (dendritic-web) without degrading solar cell performance.

Briefly, the program consists in (1) establishing a matrix of those impurities which produce deep levels in silicon, (2) the growth of doubly and multiply-doped silicon Czochralski ingots and dendritic-web crystals containing a baseline boron dopant and specific impurities chosen from the matrix, (3) assessment of these crystals by a battery of chemical, microstructural, electrical and solar cell tests, (4) correlation of the impurity kind and level with crystal quality and device performance, and (5) delineation of the tolerable impurity regimes for crystal growth and useful silicon solar cell performance.

In adopting this approach we realize there are several other areas which, though important, must initially be given lower priority and which probably can be attacked effectively only after a data base

is established. These areas include, for example, the effects of varying base resistivity and type, possible synergistic behavior of multiple contaminants, identifying specific mechanisms of cell degradation, and the modification of cell fabrication processes to increase cell impurity tolerance. Concentrated effort on these problems clearly is beyond the scope of the program, but some insight into each should develop as this study progresses.

2.3 Program Personnel

This program is being conducted by a team of scientists from the Westinghouse Electric Corporation and Dow-Corning Corporation whose technical responsibilities are identified below;

Westinghouse Research Laboratories

Dr. R.H. Hopkins -- Technical Manager and Dendritic Web Studies

Dr. P. Rai-Choudhury -- Device Diffusion

Mr. J. R. Davis -- Solar Cell Testing and Analysis

Mr. P.D. Blais -- Lifetime Studies, Photolithography and Metallization

Dow-CorningCorporation

Dr. J.R. McCormick -- Czochralski Ingot Preparation and Evaluation.

Dr. R. Mazelsky, Westinghouse, has administrative responsibility for the program.

3. PROGRAM SEQUENCE AND EXPERIMENTAL METHODS

3.1 Material Evaluation Sequence

The general features of material flow, sample evaluation and data collection for the experimental program are depicted in Fig. 1. As the figure illustrates, silicon material (whose impurity type and level are defined by an impurity matrix) flows through a sequence of process steps and is subjected to various evaluations -- chemical, microstructural, electrical and device tests -- as each step is completed.

The decision-point comparisons indicated on the flow diagram form a set of evaluation criteria for the material. The preliminary evaluation criteria include microstructural checks for dislocations and defects in the ingot (defects $< 5 \times 10^4$) and wafer, acceptable resistivity variation for the ingot ($\rho = \rho_o \pm 50\%$) and spreading resistance of the wafers and feedback adjustments to the impurity matrix based on solar cell efficiencies ($n < 6\%$ decrease impurity level; $n > 12\%$ increase impurity level; $6\% < n < 12\%$ increase or decrease slightly). The criteria for impurity levels are designed to delineate impurity ranges producing modest efficiency degradation and are further based on the assumption that even cheap silicon solar cells must have relatively high efficiency (at least 12%). It is expected that the initial evaluation criteria will be modified and expanded based on the data developed during the program.

The data collected from ingots containing a given impurity and concentration will be used to adjust the impurity matrix (Section 2.2) through a set of iterations aimed at bracketing the tolerable solar cell impurity level. The accumulation of such information for each impurity, and to the extent possible combinations of impurities, will form the

basis (along with potential cost tradeoffs) for defining solar grade silicon at the end of the program.

Some other important features of the material flow and evaluation should also be noted in Fig. 1. A set of baseline (standard) wafers of common origin will be processed with each group of wafers from doubly or multiply-doped ingots. This provides a control on the process. Moreover, corroborative measurements on solar cells fabricated by Westinghouse will be carried out by NASA-Lewis Research Center. Finally, a sampling of material will be provided to JPL for independent evaluation: (1) Wafers from the seed and tang end of each doubly and multiply-doped crystal for metallographic analysis and evaluation; (2) solar cell blanks from each ingot for processing, and (3) solar cells processed by Westinghouse for corroborative testing by JPL.

In the sections to follow we describe in some detail the major components of the overall program, the experimental procedures for specimen evaluation, and the results of the first three-months effort on this program.

3.2 Impurity Matrix

A multi-dimensional matrix is required to completely define the acceptable parameters for solar-grade silicon. For example, parameters which may affect solar cell performance include (1) donor/acceptor concentration, (2) concentration of impurities producing deep levels (traps), (3) impurity species producing specific deep levels, (4) structural defects including impurity clustering, and (5) interaction of all of the above items. This program is primarily aimed at establishing the acceptable concentration of those impurities which produce deep levels in the forbidden band-gap (traps). Based on current technology of solar cell fabrication, and the limited period in which to complete the program, an acceptor concentration of $2.5 \times 10^{15} - 7 \times 10^{15}$ atoms per cm^3 has been selected both for the baseline silicon and for the process standards to be utilized during the entire program.

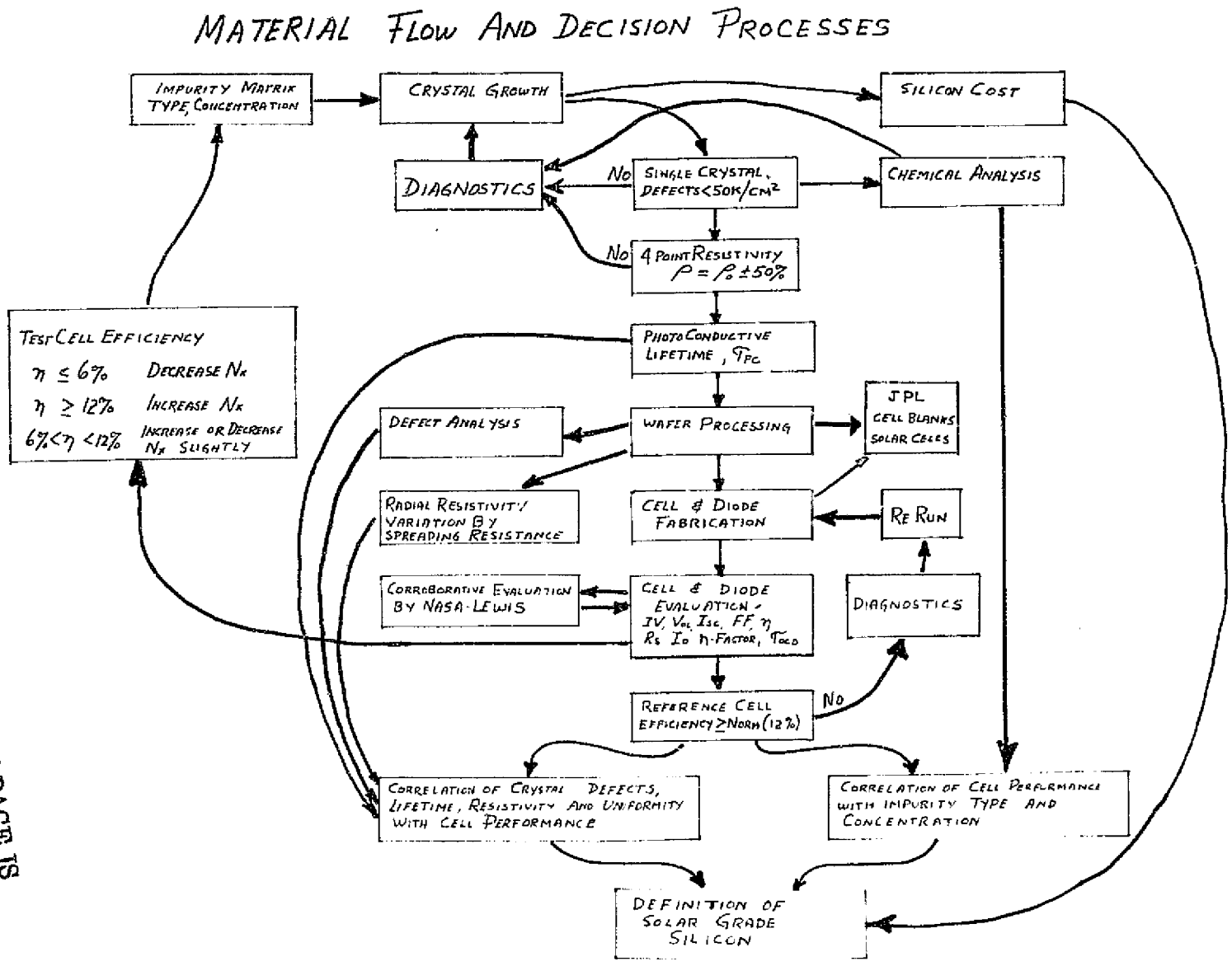

Figure 1. Material Flow and Test Sequence for the Experiment Program

All material prepared for evaluation will be doped into the above impurity range using boron as the acceptor impurity. This choice has the advantage that the resistivity range for the baseline material is sufficiently low to insure excellent cell performance from baseline material while being sufficiently high to assure that resistivity will be relatively independent of trap concentration. The use of boron, with its segregation coefficient near unity, also provides a high degree of acceptor uniformity along the length of the ingot.

The second impurity element/(trap) concentration matrix, Fig. 2, is comprised mainly of transition elements which are commonly observed in metallurgical-grade silicon and which produce deep impurity levels (traps) in silicon thus decreasing minority carrier lifetime. Initially, first generation ingots with baseline resistivity and transition element impurity concentration in the 10^{15} to 5×10^{15} atoms/cc range will be prepared.

The choice of the initial transition element impurity range is based on several factors:

- results obtained in previous programs,
- the concentration range is near the solid solubility limit of many of the elements of interest in silicon,
- at 5×10^{15} atoms/cc, the required melt concentration approaches conditions conducive to constitutional supercooling and attendant polycrystalline growth,
- the concentration is in a range sufficiently high to permit the establishment of reliable mass spectrographic standards for future comparison.

Ten ingots, each doped with a different impurity element, first will be prepared. Based on crystalline quality and device performance, the impurity concentration in the second generation ingots will be either increased or decreased. Poor device performance or an inability to grow single crystal will establish a particular impurity concentration as

IMPURITY MATRIX

Concentration Range

Impurity Element	$< 10^{14}$	5×10^{14} To 1×10^{15}	1×10^{15} To 5×10^{15}	5×10^{15} To 1×10^{16}	$> 10^{16}$
Cr					
Mn					
Cu					
Ni					
Fe					
Ti					
V					
Mg					
Zn					
Zr					

1st Generation

unacceptable. A second generation ingot will then be grown at a lower impurity concentration. If necessary, a third generation ingot will be prepared with a higher or lower concentration than second generation material based on test results. Thus, the impurity matrix will undergo continuing revision as the program progresses.

As third generation ingot preparation nears completion, multiply-doped ingots will be grown. The ingots will be doped with two or more transition elements. Again, the concentration of these impurities will be determined by the results of preceeding experiments.

3.3 Ingot and Web Preparation

All ingots are being prepared by Czochralski crystal pulling. The method offers several advantages: 1) a relatively flat crystal dopant profile (a factor of two variation can be obtained) for the first fifty percent of ingot pulled from the melt, 2) impurities can be added either before or after charge melt down, and 3) growth conditions can be varied significantly in a controlled fashion.

A modified NRC 2805 crystal pulling furnace capable of accepting 1.5 Kg charges is being used to prepare the ingots for this program. The system employs a graphite resistance heater. The quartz crucible is held in a graphite cup. Separate graphite components are maintained for each impurity element under investigation. Prior to crystal growth, the heating element/crucible system is given a four hour vacuum bake-out at 1500°C. After cool-down the crucible is loaded with an 860 gram charge of semiconductor grade silicon nuggets. Acceptor concentration is controlled by adding a silicon pellet (DOPSIL*) containing the desired boron concentration. The second impurity (transition element) is added to the crucible either before or after melt-down. Those impurities with high vapor pressure or low melting points are added to the molten silicon after melt-down and immediately prior to growth to avoid potential dopant loss from the melt.

*Dow Corning Trademark

The amount of impurity chosen for a given run is calculated from the known impurity segregation coefficients, Table 1, on the assumption of normal segregation during growth. A sample of the melt is taken following crystal growth, and analyzed to determine melt impurity concentration and to assure that significant impurity loss from the melt did not occur.

Crystal growth is generally carried out for a sufficient period of time to produce a single crystal ingot at least six inches in length. Growth parameters such as growth rate, crucible rotation, seed rotation, and inert gas composition are maintained as constant as possible both during growth and from ingot to ingot. A low growth rate is used to assure that segregation effects may be approximated by use of the equilibrium segregation coefficient. A typical data sheet illustrating the data collected for each experiment including electrical, structural and chemical characterization is illustrated in Fig. 3.

Besides the Czochralski crystals grown to evaluate the effects of impurities on silicon crystal quality and solar cell properties, a set of sheet crystals, more limited in number, will be grown by the Dendritic Web process to isolate the effects of impurities on rapidly grown silicon single crystal sheet. The choice of kind, number and level of impurity dopants will be determined on the basis of the results obtained by evaluating initial sets of Czochralski crystals. The emphasis will be on doubly-doped web crystals although the growth of multiply-doped sheet may also be attempted depending on the cell evaluation of the Czochralski crystals.

The web crystals will be grown from silicon starting material provided by Dow Corning Corporation from the same master batches used to grow the Czochralski crystals. This will facilitate comparison of sample data. Specimens from the head and tail of the web sheets grown in a laboratory apparatus will be chemically analyzed in the same manner as the Czochralski material (Section 3.4). The microstructural, electrical,

Table 1. Characteristics of Dopant Impurities

Dopant	Form	Purity %	Melting Point (°C)	Temperature For 1 mm Vapor Pressure (°C)	Segregation Coefficient
Chromium	Pellets	99.999	1900	1504	10^{-5}
Manganese	Flake	99.99	1244	1251	10^{-5}
Copper	Zone Refined Ingot	99.9997	1083	1628	4×10^{-4}
Nickel	Sponge/ Wire	99.999/ 99.97	1455	1884	0.8×10^{-5}
Titanium	Crystal	99.95	1668	∿2500	10^{-5}
Vandium	Dendrite	99.9	2190	∿2550	10^{-5}
Zinc	Rod	99.999	419	487	10^{-5}
Zirconium	Foil	99.99	2127	2450	10^{-5}
Iron	Sponge/ Ingot	99.999/ 99.999	1535	1783	0.8×10^{-5}
Magnesium	Ingot	99.99	651	605	$\sim 10^{-3}$

Figure 3

SILICON INGOT DATA SHEET

Run # 1286 Date 11/17/75 Mach. # C-12 Cryst. # W-004-CR-001

Operator J.H. Seed Orient. 111 Targ. Dia./Ln. 1.25" x 6"

Loading Data

Charge ID 1006453 Charge Wt. 852.8 g

Crucible ID 4 x 5

Targ. A/D Type/Conc. Boron/4.5×10^{15} A/D Source/Conc./Wt. Dopsil/2×10^{18} /

Targ. Imp.(1) Type/Conc. CR/1×10^{15} Source/Conc./Wt. Pellets/10^{20}/3.15 g

Targ. Imp.(2) Type/Conc. _____ Source/Conc./Wt. _____

Targ. Imp.(3) Type/Conc. _____ Source/Conc./Wt. _____

Comments: Chromium 99.999% Pure Pellets

Melt Down

Gas/Gas Flow/Vacuum(CFH/In) Argon/15/30 Cruc. Pos. 0

Crucible Rot. 3.3 rpm Start Time 8:10 Time Melted 9:15

Comments:

Growth Data

Gas/Gas Flow/Vacuum(CFH/In) Argon/15/30 Pressure _____

Crucible Pos. 0 Crucible Rot. 3.3 rpm/13 rpm

Time Growth Initiated 0930 Time Growth Comp. 12:35

Pull Rate 2.75 inch/h Lift Rate 8

Comments: After six inches of single crystal growth polycrystalline growth began. Ingot appears to have relatively high metal concentration in tang end.

Analytical Data

Resistivity	Center	R/2	Edge
Seed	4.65	4.6	4.40
Tang	4.30	4.35	4.30

Calculated Impurity Conc. (1) 1×10^{15} + (2) _____ (3) _____

Mass Spec. Analysis (1) 1×10^{15} (2) _____ (3) _____

Crystallography	Seed	Tang
EPD	$500/cm^2$	$1.5 \times 10^5/cm^2$*

Comments:

* Measurement made near polycrystalline region. Slices are from seed area and 500-1000/cm^2 EPD should be indicative of slices.

+ Based on wt. of added to melt; value of $.82 \times 10^{15}$ calculated based on analysis of crucible

and device evaluation of the web material also will be performed in essentially the same manner as the Czochralski wafers, again to facilitate direct comparisons.

3.4 Ingot and Web Evaluation

The basic scheme for ingot and web evaluation is illustrated in Fig. 4. Each pulled crystal is first checked to assure adequate dimensions. Slices are then removed from the seed and tang ends of the ingot. The seed slices are taken after the ingot has reached its full diameter (i.e., after the transition region). One slice from the seed and tang end of each ingot (web) is chemically polished and given a Sirtl dislocation etch to evaluate crystal structure. Although a dislocation density of 5×10^4 is considered as acceptable, most of the ingots so far produced exhibit $< 10^3$ cm^{-2} dislocation densities. Resistivity measurements are made at the center and R/2 position of the seed and tang end of the ingot section. The resistivities of all the ingots prepared have been within the 2 ohm-cm to 6 ohm-cm target range.

One slice from the seed end of the ingot is processed for mass spectrographic analysis. The transition region of the ingot and tang end of the ingot are retained for use in neutron activation analysis. Additional slices are retained for autoradiography, infrared transmission, or other measurements as required. The results of the analysis of the crucible remains are also used in evaluating the growth process.

Samples having adequate crystalline structure, proper resistivity, and for which analysis of the crucible remains is in agreement ($\pm$ 30%) with the amount of dopant added to the melt, are processed into slices by ID sawing.

The analytical data is provided with the slices for solar cell processing and evaluation. Based on the sum total of information available on cell performance, material characteristics, and growth parameters, second generation, third generation and multiple-doped ingots (webs) are prepared to permit determination of tolerable impurity concentrations.

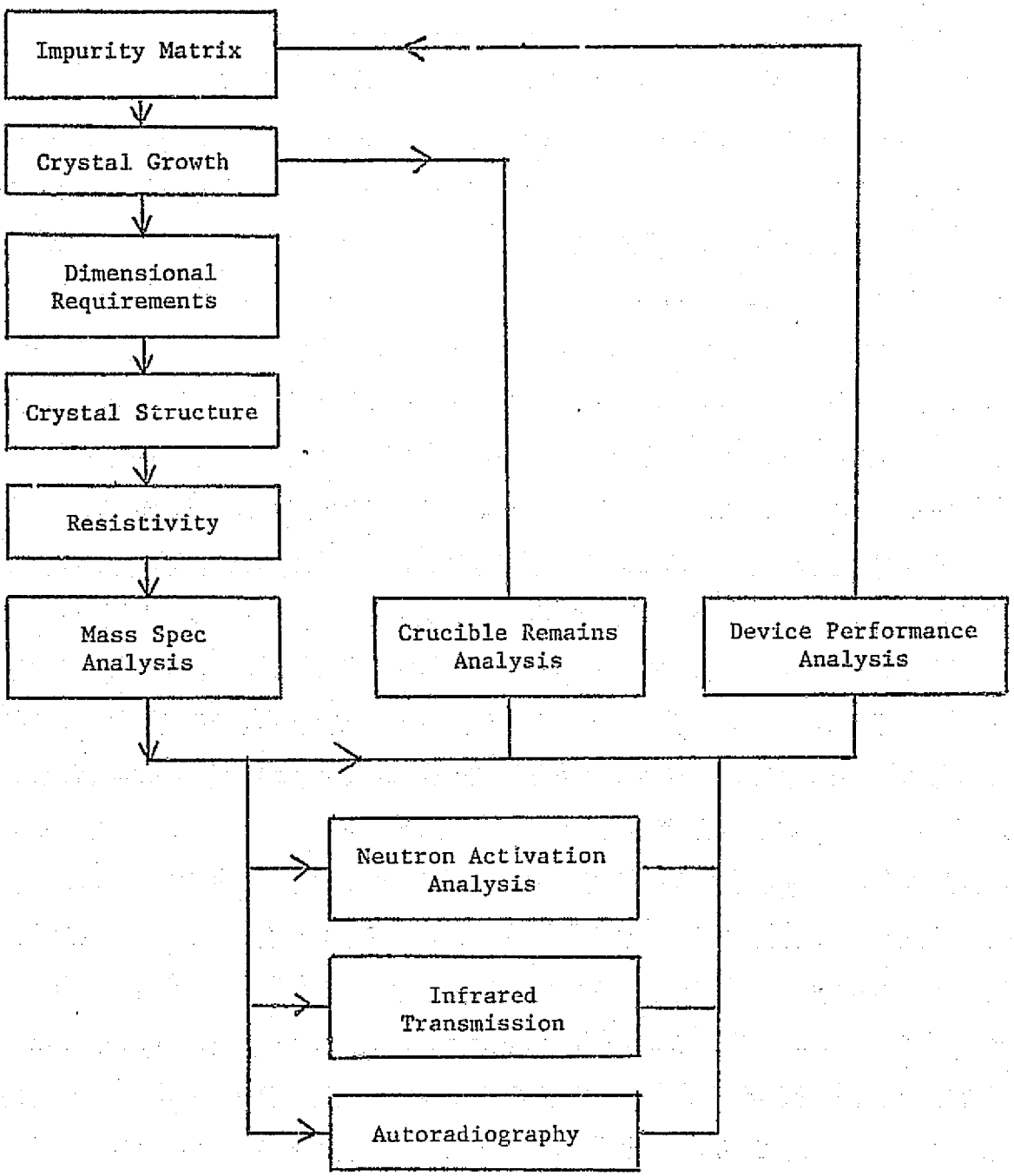

Figure 4. Flow Diagram of Ingot Preparation and Analysis.

3.5 Silicon Wafer Evaluation

Wafers from ingots and dendritic web which successfully pass the screening and evaluation described in Section 2.4 are themselves further evaluated prior to cell fabrication. The testing consists primarily of microstructural examination, spreading resistance and bulk lifetime measurements.

3.5.1 Microstructural Evaluation

Both Sirtl and Secco d'Aragona etches are used in combination with optical microscopy to reveal growth and process-induced defects. Excessive defect concentrations in the wafers will be cause for rejection from further evaluation. Lang X-ray topography is being used on a selected basis to further assess wafer fine structure.

3.5.2 Spreading Resistance

Spreading resistance measurements will be made with a Mazur Spreading Resistance probe to assess the spatial uniformity of carrier concentration typical of the ingots. Again, the data will be correlated with cell measurements to give insight into the manner in which impurities degrade cell performance.

3.5.3 Lifetime Measurements

We expect to use various lifetime measurements methods to evaluate wafers prior to and after solar cell processing and also to study the solar cells themselves. For this reason and because the lifetime measurements must be interpreted in the context of the measurement techniques employed, some elaboration of the approach we have taken is warranted here.

Carrier pairs are generated in the bulk of a solar cell by the absorption of photons energetic enough to excite electrons from the valance band into the conduction band. The majority carriers created are accommodated by relaxation of all the other majority carriers in a

period of about 10^{-13} seconds. In contrast, the generated minority carriers are vulnerable to recombination with the populous majority carriers. Thus, to produce an external current from the cell, minority carriers must survive a random diffusion walk from their generation points to the metallurgical junction. The survival probability is determined by the minority carrier diffusion length, $L = \sqrt{D\tau_r}$, and the necessary diffusion distance. The output current for a solar cell is therefore highly dependent on recombination lifetime, τ_r (and inversely proportional to the density of recombination centers near the center of the energy gap). Primary recombination centers are imperfections in the silicon lattice, impurities, or chemical complexes. Electrons are the minority carriers of primary interest in an N^+/P solar cell.

The minority carrier lifetime is generally measured by creating a momentary nonequilibrium in carrier concentration and then observing the time for equilibrium to be re-established. The nonequilibrium condition can be produced by injection of excess minority carriers ($np > n_i^2$), or depletion of the minority carrier level ($np < n_i^2$). The injection method measures the recombination lifetime, τ_r, and is thus directly relevant to solar cell performance. The recombination lifetime depends on the injection level so our study will be restricted to low injection levels, ($\Delta n << N_a$), the pertinent condition for solar cells used without high ratio concentrators.

When the excess carriers are injected by applying a pulse of light with $h\nu \geq Eg$, the technique is called the photoconductive decay method (PCD). The excess carriers are monitored by measuring the electrical conductivity of the sample as a function of time. This classical technique, outlined in ASTM Standard F28-75, will be the primary test method. When the excess carriers are electrically injected by means of p-n junction whose open circuit potential is then monitored, the method is termed Open Circuit Decay (OCD). The OCD Method will be used on processed wafers for correlation with photoconductive decay measurements.

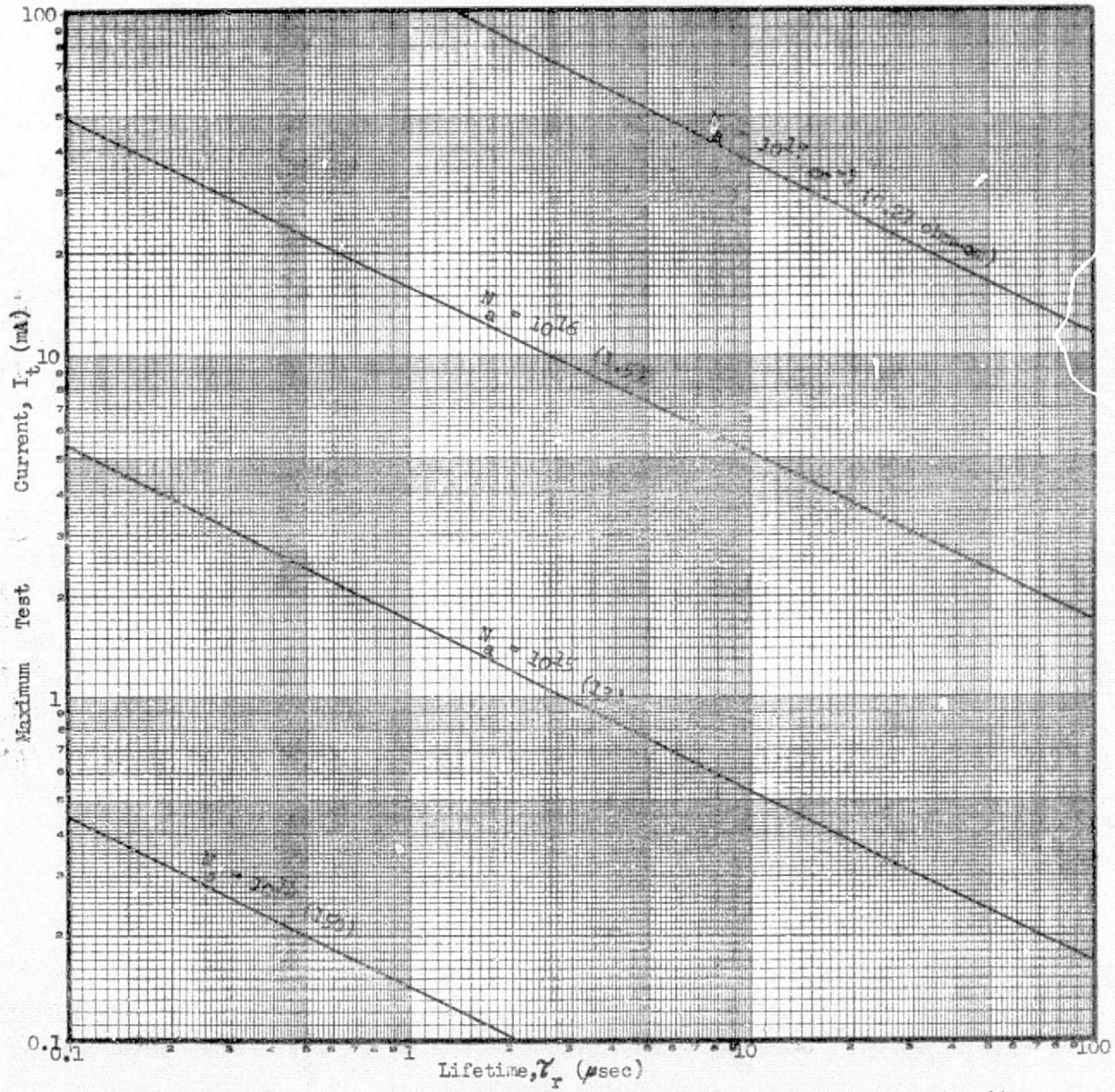

Fig. 5. Maximum test current, I_t allowed for negligible distortion of the minority carrier distribution by the resulting electric field.

Recombination within the bulk of the silicon is augmented by recombination which occurs at the surface, the two effects combining to produce an effective recombination lifetime, τ_r'. While the output of a solar cell is probably related more to τ_r', knowledge of τ_r, the bulk value, is also desirable since this lifetime is affected by impurity content and heat treatment. Since photoconductive decay measures τ_r', surface recombination effects must be separated to obtain τ_r.

The excess minority carriers obey Eq. (1) for the case of a uniform electric field, E_x in the x direction. The contribution of the last two terms in Eq. (1) must therefore

$$\frac{\partial n}{\partial t} = -\frac{n}{\tau_r} - \mu E_x \frac{\partial n}{\partial x} + D\nabla^2 n \qquad (1)$$

be either minimized or mathematically accounted for in order to obtain the value of τ_r. The second term is easily reduced to insignificance by merely reducing the electric field which is due to the current used to measure the conductivity. The critical field is[1]

$$\frac{(\mu E)^2}{4D} << \frac{1}{\tau_r} + v_{ijk} \qquad (2)$$

where μ is the mobility of the carriers, D is the diffusivity and v_{ijk} is the surface recombination velocity term for the ijk^{th} mode of the Fourier Series necessary to account for the finite boundaries. For the most conservative case where v_{ijk} is assumed equal to zero ($v_o = 0$) and a minimum inequality ratio of 10 is necessary, Eq. (2) may be simplified to,

$$E \leq \frac{1}{10}\sqrt{\frac{4kT}{q\mu\tau_r}} \qquad (3)$$

Equation (3) is plotted in Fig. 5 for a silicon test sample 0.0254 x 1.0 x 1.0 cm. The last term in Eq. (1) is dependent on the surface recombination velocity because the local loss in carriers produces

a divergence in the carriers. The problem is particularly acute for thin silicon specimens such as wafers because the volume to surface recombination ratio is small. The problem can be resolved in two ways: (1) Use a rigorous mathematical analysis[1] with a known surface recombination velocity (normally ∞), and (2) Experimentally reduce v_o and extrapolate the value of τ_r. The first approach fails for thin specimens, since the effective lifetime, τ_r', becomes too short for accurate measurement with $v_o = \infty$. The latter method will be used during this project.

3.5.3.1 Recombination Lifetime

Photoconductive decay measurement equipment has been set up to determine the recombination lifetime in thin silicon wafers. The equipment, schematically depicted in Fig. 6, uses a silicon test sample 0.0254 x 1.0 w x 2.0 ℓ cm. Each sample is prepared by first evaporating 5000 Å of aluminum on one side of the specimen, and then using photoresist to delineate four Kelvin type ohmic contacts. Contact bars are 0.076 cm wide and extend the full width of the sample. The voltage sensing contacts are spaced 1.0 cm apart, and the current application contacts are spaced 0.127 cm beyond the voltage sensing contacts. All contacts are sintered at 500°C for 10 minutes in N_2 to reduce interfacial SiO_2. The test samples are given a light etch in $HF:HNO_3$ (1:10) to reduce the surface recombination velocity. The light shield, designed to eliminate photovoltaic effects at the contacts, has an opening 0.5 cm wide and the ratio of the illuminated length, ℓ, to the total electrical length, ℓ_o, is 0.5. This factor is used via Eq. (4) to verify that the injection ratio[2]

$$\Delta n/n = \frac{b}{b+1} \quad \frac{\Delta v/v}{\ell/\ell_o - \Delta v/v} \tag{4}$$

($\Delta n/n$ = ratio of injected minority carriers to majority carriers
b = mobility ratio of majority to minority carriers
$\Delta v/v$ = relative change in photovoltage to dark voltage)

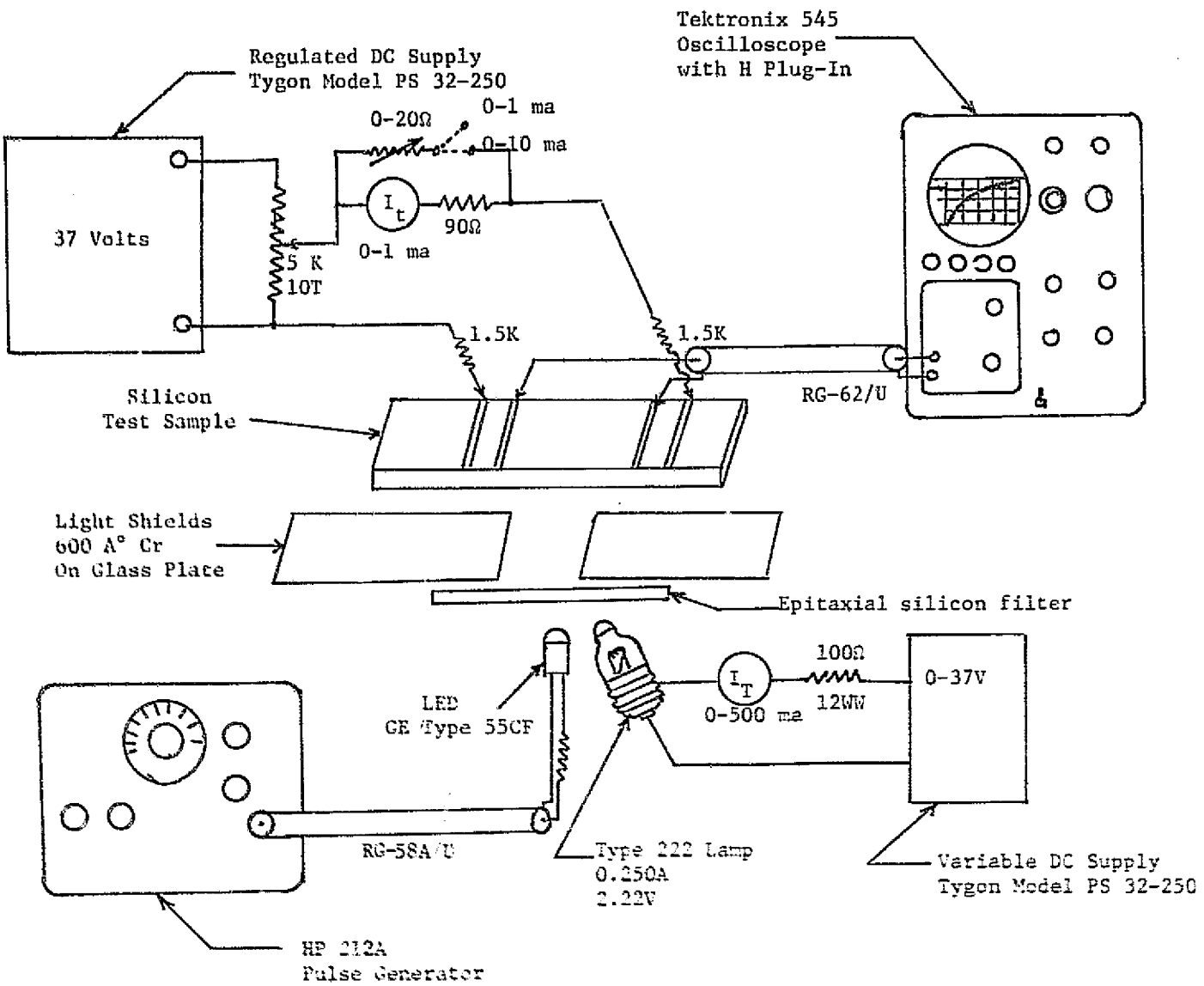

Fig. 6. Schematic diagram of photoconductive decay lifetime measuring apparatus.

does not exceed the low injection conditions. 1500 ohm, 0.25 W carbon resistors are used near probe tip to make an effective constant current Thevinew Generator. The resistors are placed at the probes in order to eliminate the effects of parasitic capacitance in the current leads. A constant current rather than constant voltage system was chosen since the current sensing resistor in a constant voltage system linearizes the system unless the sensitivity is reduced toward zero.

The pulsed light source, an LPE gallium arsenide IR-emitting diode, GE type LED 55 CF, emits at a peak wavelength of 940 nm, very near to the absorption band edge for silicon. The absorption coefficient is approximately 250 cm^{-1} [3] so the 1/e depth is 40 μm, probably sufficient to prevent accentuating the surface recombination problem. The LED has a fall time (100-10%) of 200 ns which permits lifetime measurements down to about 1 μsec. The spectral bandwidth to 50% amplitude is 60 nm. An epitaxial silicon film on sapphire filter is used to selectively skew the spectrum by absorbing the shorter wavelengths. The LED leads are also purposely left long in order to take advantage of the thermal coefficient of spectrum change (+ 0.28 nm/°C).

A conventional tungsten lamp with built-in focussing lens is used to fill deep traps, which are especially troublesome when present in p-type silicon. The experimental apparatus, Fig. 7, was recently completed and has been used for a limited number of preliminary measurements which are described in Section 4, along with OCD data developed from processed solar cells.

3.5.3.2 Generation Lifetime

Supplementary measurements of generation lifetime were made on selected baseline ingot wafers by the deep depletion MOS technique. The unprocessed wafers were oxidized at 25°C by anodizing in a mixture of 100 ml tetrahydrofurfuryl alcohol, $C_5H_{10}O_2$, and 2.2 gr potassium nitrite, KNO_2. An oxide growth rate, 35-44.5 Å/min, was controlled by the current density to a final thickness of 1166 ± 95 Å. Aluminum electrodes were applied by electron beam evaporation in a high

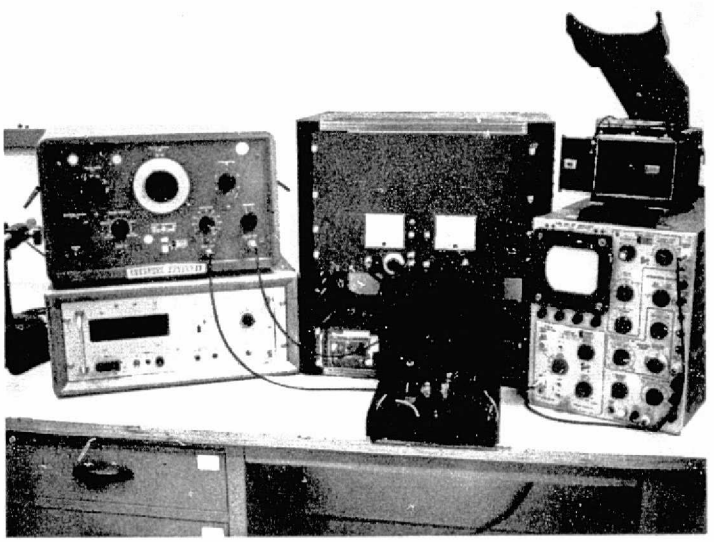

Fig. 7. Photoconductive decay apparatus.

vacuum followed by photoresist delineation. A guard ring MOS structure was required since the positive charge density within the anodic oxide was sufficient to invert p-type silicon with an acceptor concentration, N_a, of 8.5×10^{15} cm^{-3}.

The results of the measurements appear in Section 4.

3.6 Solar Cell Design and Fabrication

Solar cells and a number of diagnostic devices are fabricated on ten wafers selected from the ends and center of each silicon ingot (or web). Five baseline (standard) wafers also are processed simultaneously with each batch of doubly or multiply-doped wafers to assure processing constancy and control. Details of the cell design, processing, and diffusion characteristics are described below.

3.6.1 Solar Cell and Test Pattern Design

The original three finger cell proposed in the Program Plan has been modified to improve the fill factor and cell efficiency. (We have also reduced the silver metal thickness from 5 to 2 μm to achieve improved resolution in photolithography.) The new geometry, Fig. 8, uses a five-finger grid covering 5.4% of the cell area. Reference cells using this design and without AR coatings have reached 10% efficiency and fill factors around 79% under AM1 equivalent quartz-iodine illumination, viz. Section 4 and Appendix 2.

The test pattern directly under the cell in the figure is used to examine sheet resistivity and contact interface resistance. This structure was also modified to improve the resolution of these measurements. Additional test patterns are included to measure the diffused layer sheet resistance and various diode properties; four miniature solar cells are also available if needed to examine wafer uniformity.

The cell design has not been optimized for high efficiency but rather for processing ease and reproducibility and as a test vehicle for examining the effects of the various impurities added to the silicon. The present cell design is now believed to be adequate for these purposes.

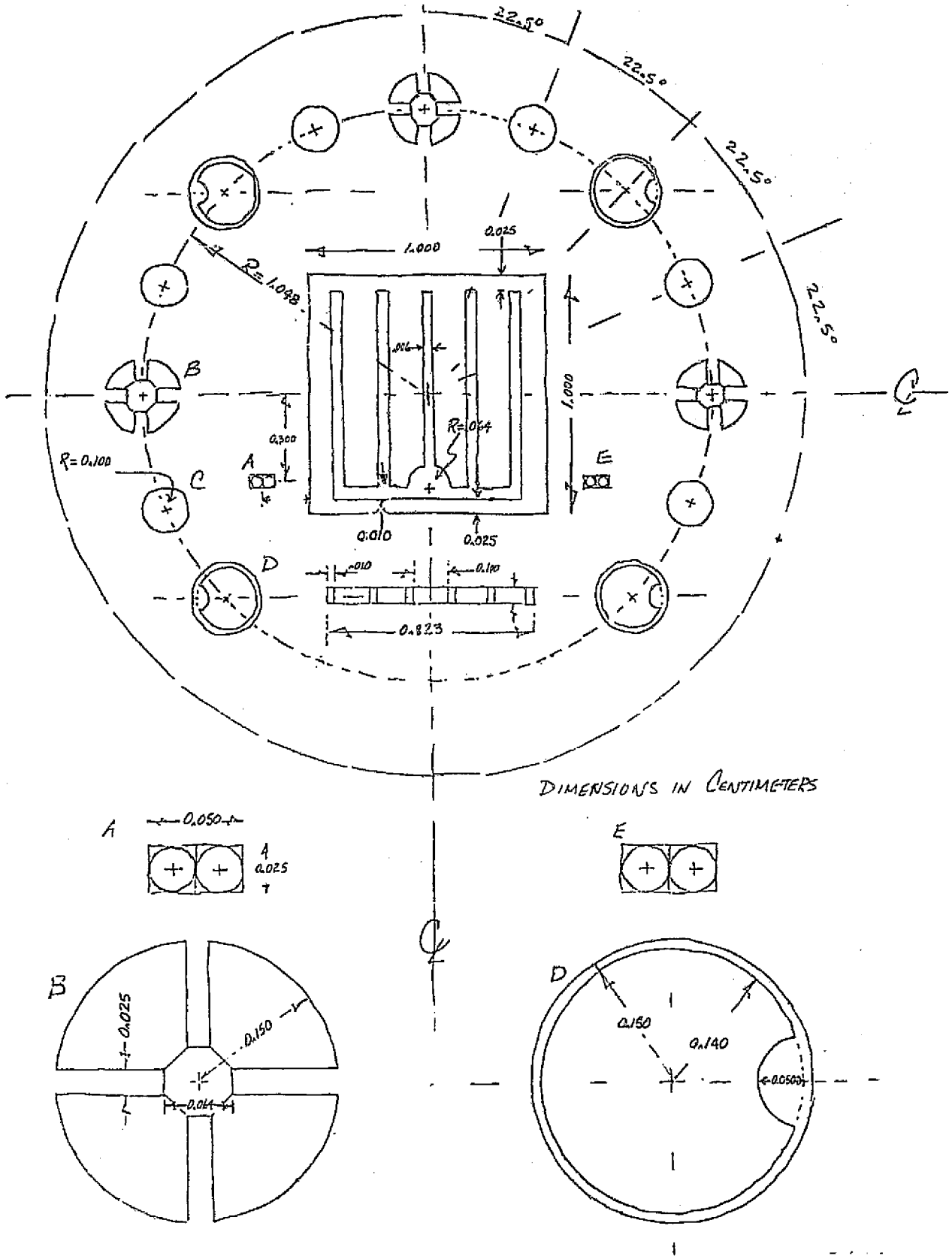

Fig. 8. Solar cell mask design.

3.6.2 Solar Cell Fabrication

The standard cell processing sequence we use involves some sixteen steps outlined in the sample process log, Fig. 9. Below we highlight some of the more important aspects of the process: diffusion heat treatment, the diffusion profile, and metallization.

3.6.2.1 Diffusion

The 1x1 cm test cells and anxillary structures are formed by open tube diffusion of $POCl_3$ at 825°C (our past experience indicated that $POCl_3$ diffusion sources exhibited superior gettering properties compared to PH_3). Suitable adjustment of the gas flow rate, dopant partial pressure and diffusion time provides sheet resistivities ranging from 40 to 120 ohms/□ and reproducible to ± 2%. Initially, our target was a 60 ohm/□ sheet resistivity, 5 x 10^{19} cm^{-3} surface concentration and 0.4 μm junction depth.

3.6.2.2 Diffusion Profile

After several attempts to determine the surface concentration and junction depth by the spreading resistance technique, we concluded that the equipment was not suitable for measurements on junctions as shallow as 0.5 μm. Angle lapping and staining also failed to reveal the exact junction depth because we could not ascertain just where the bevel commenced. Standard staining techniques involving HF and high intensity light darkens the P^+ area, not the diffused N^+ region of interest to us.

The surface concentration and the junction depth was finally evaluated by means of the incremental sheet resistance methods first described by Tannenbaum.[4] The average conductivity, $\bar{\sigma}$, of a thin sheet of removed silicon is given by,

$$\bar{\sigma} = \left(\frac{1}{\rho_{n-1}} - \frac{1}{\rho_n}\right) \frac{1}{\Delta x_n}$$

where ρ_{n-1} is the sheet resistivity prior to removing the n^{th} layer of silicon, and ρ_n is the sheet resistivity after etching a thin layer of

Fig. 9

Start Date:	PROCESSING LOG	Page	Run or Sample
Material:			
Quantity:	Engr.		

Date Tech.	*Process	Special Instructions, Measurements, etc.	Disp. C	Disp. E
	LAP (1)	Wafer Thickness		
	CLEAN (2)	Trichloroethylene, Acetone, Methanol		
	CHEM POLISH (3)	Surface Quality Wafer Thickness		
	CLEAN (4)	H_2O_2 - NH_4, H_2O_2 - HCℓ		
	POCℓ (5) DIFFUSION	Source Temp. = 0°C Flow Rates 200 cc/min - N_2/Source; 1560 cc/min - N_2 Carrier 62.5 cc/min O_2		
		Diffusion X_j = C_o = Temp. 825°C Time 50 min. ρ_s =		
	P-ETCH (6)	H_2O : HF : HNO_3 Time = 300 : 15 " 10 (Remove all oxides)		
	CLEAN (7)	H_2SO_4 : H_2O_2 87°C, 5 min 10/1 H_2O/HF Dip 10 sec		
	METAL (8)	Top Side Only Ti 500 Å 50 Å/sec Pd 300 Å 50 Å/sec		
		Ag 20000 Å 60 Å/sec		
	PHOTO-RESIST (9)	Mask #1 (contact grid) Waycoat IC, 4000 rpm, h = 1.7 μm Exposure time = 3 sec (I_d = 0.2 μa)		
	ETCH (10) METAL	Ag-50-50 H_2O_2 & Ammonium Hydrox.-10-15 sec. Pd-Warm 40cc H_2O + 30cc HCℓ + 10cc HNO_3-5 sec. Ti-150cc H_2O + 60cc HCℓ + 30cc Ammonium Fl. 5 sec.		
	LAP (11) BACK	Check Conductivity Type		
	CLEAN (12)	H_2SO_4 at 100°C - 5 min Rinse in D.I. H_2O.		
	METAL BACK (13)	Ti - 500 Å - Pd 480 Å Ag - 20 KA		
	SINTER (14)	Temperature Time 550°C 15 min/H_2		
	PHOTO-RESIST (15)	Mask #2 (Mesa) Waycoat SC, 6000 rpm, h - 4.0 μm Exposure time = 15 sec (I_a = 0.6 μa), Apeicon wax back side		
	ETCH (16) SILICON	44 cc HF + 26 cc HNO_3 + 78.5 Acetic 25°C, Etch time = 10-15 sec Etch silicon between 5 to 8 μm deep, Talystep _____μm.		
	TEST (17)			

* SEE DETAIL PROCESS INSTRUCTIONS

thickness Δx_n. The sheet resistivity was measured by the standard 4 point probe technique with a probe spacing of 0.025 in. The anodic oxidation technique described in Section 3.5.3.2 was used to remove silicon layers of precisely measurable thickness. The silicon removed by each oxidation step was both calculated and measured to be 318 Å. (The impurity concentration is determined from the average conductivity, $\bar{\sigma}$, by the use of Irwin's[5] ρ-N plot.)

The surface concentration was measured for several samples, Table 2. The experimental diffusions were performed as simple attempts to reduce the surface concentration.

Table 2

Surface Concentration Measurements for Diffused Junctions

Sample Identification		Surface Concentration (cm^{-3})
Material Lot	Diffusion Lot	
W002 Baseline	W005Mn[1]	3.7×10^{20}
W002 Baseline	W006NI001[1]	4×10^{20}
W002 Baseline	Experimental[2]	2.6×10^{20}
13 Ω-cm Semimetals	Experimental[3]	2.5×10^{20}

1. Standard Diffusion Cycle; 50 min. @ 825°C, N_2 (carrier) = 1560 cc/min, O_2 = 62.5 cc/min, N_2 (source) = 200 cc/min, $POCl_3$ = 0°C.
2. Experimental; 10 min. @ 825°C deposition (same gas flows as standard), Soak 2 hrs, N_2 (carrier) = 1560 cc/min, O_2 = 62.5 cc/min.
3. Experimental; 5 min. @ 825°C deposition (same gas flows as standard). Strip deposition oxide, drive-in 40 min. @ 825°C, N_2 = 1560 cc/min, O_2 = 62.5 cc/min.

In principle the method can be used to determine the complete diffusion profile; however, continuation beyond a depth of 0.1 μm proved difficult due to damage under the probe points. The damage induced in the silicon in turn increased the junction leakage thus invalidating the boundary condition of an insulating layer. A new probe head designed to reduce lattice damage has been ordered and received. Complete profile measurements are scheduled for completion during the next period.

By removing many layers and checking for conductivity type by means of a hot probe, it has been established that the junction depth is between 0.35 and 0.42 μm. While impurity profile studies are not a primary aspect of this program, these results provide important background information. For example, if necessary, the efficiency of the baseline solar cells could probably be increased by reducing the surface concentration to approximately 5×10^{19} cm^{-3}.

3.6.2.3 Metallization Studies

The maximum power output of a solar cell is very dependent on the electrical conductivity of the metallization system used to collect the current, since the internal impedance of a solar cell is quite low (18 ohms/cm^2) and very small potential drops are significant. Al, Au, Ag, and Cu all have sufficient conductivity for useful contacts. Al is generally used on silicon devices, having advantages of low cost and the ability to reduce SiO_2 to insure intimate Al-Si contact. The heat treatment necessary for establishing minimum contact resistance can, however, severely reduce the conversion efficiency of solar cells.[6] The other candidate elements, Au, Ag, and Cu, require the prior deposition of a nucleation film such as Ti, Cr or Mo to reduce the SiO_2. Ti/Ag is normally used for solar cells in order to avoid Cu contamination and the high cost of gold. Ti/Ag contacts may become unreliable due to electrochemical corrosion of the Ti. (The Ti is anodically converted to low conductivity oxides in the presence of moisture.)

Fischer[6] developed the passivated contact system Ti/Pd/Ag which does not experience any degradation with time at 100% relative humidity. This system is based on the fact that very small amounts of Pd (less than 1%) added to Ti will shift the electrochemical potential of Ti into the passive range, with a potential nearly identical to that of Pd. For this reason we have selected the Ti/Pd/Ag metallization system for the fabrication of solar cells during this contract.

The deposition sequence is as follows. 1500 Å of Ti are initially deposited at a rate of 20 Å/sec in a four-crucible electron beam vacuum evaporator. The Pd is then evaporated to a thickness of 300 Å. We use a low-cost, high-purity Pd sponge as a source material so that the deposition rate must be manually controlled to about 3 Å/sec in order to prevent splatter. A large amount of beam sweep and dither is also employed for this reason. 2 μm of Ag is finally evaporated at a rate of 60 Å/sec with only a minimal amount of beam sweep and dither.

Silver tarnishes with time due to trace amounts of H_2S in the environment and experiments were performed to alleviate this problem by evaporating 1000 Å of gold over the Ti/Pd/Ag contacts. Attempts to photoresist and chemically delineate this system were unsuccessful due to extreme difficulty in etching the film. The difficulty was attributed to the diffusion of Au into the Ag layer during the deposition process. Substrate cooling could be used to minimize this problem, but was not implemented since extensive tooling would be required and the benefit of an Au cover film is not considered vital to the main objectives of the program.

The solar cell metallization thickness is a compromise between IR losses and resolution capability. Very thick films lower cell efficiency because the active area is reduced by the need for wider contact grids. Initially, the Ag film thickness was set at 5 μm, on the basis of past experience and preliminary calculations which indicated negligible IR losses in completed cells.

We did conduct a small optimization study to evaluate the effect of reduced metallization thickness on cell performance. Ten wafers of baseline (standard) lot W003 were diffused in accordance with our standard $POCl_3$ procedure. The lot was then divided into 4 groups of wafers, and each group was metallized with a different Ag thickness varying from 1 to 4 μm. The cells were individually identified and then returned to a single combined lot for simultaneous further processing into completed cells.

Table 3

Effect of Ag Film Thickness on Cell Parameters

Group No.	Ag Thickness* (μm)	V_{oc} Volts	I_{sc} mA	F.F.	Efficiency %	R_s† (Ohms)
1	1.1	0.555	22.1	.782	9.59	.35
1	1.1	0.555	22.1	.753	9.24	.35
1	1.1	0.558	21.8	.767	9.33	.45
2	2.1	0.555	21.8	.771	9.33	.45
2	2.1	0.555	22.5	.768	9.59	.50
3	3.0	0.546	21.9	.642	7.68	.35
3	3.0	0.538	21.9	.623	7.34	.35
3	3.0	0.535	21.9	.606	7.10	.35
4	4.2	0.555	22.5	.760	9.49	.30
4	4.2	0.555	22.1	.774	9.49	.35

*Ti thickness varied between 1500 to 1800 Å and Pd thickness varied between 260 to 380 Å.

†Series resistance determined by incremental cell voltage change due to forward test current variation between 180 to 200 mA.

The results of the study, Table 3, indicate that none of the important solar cell parameters related to series metallization resistance vary as the Ag film thickness is increased from 1.1 to 4.2 μm. The

most important parameter, the effective series cell resistance, R_s, was constant for all the groups, including group 3. (I-V measurements under darkened conditions later showed that excessive p-n junction leakage current was responsible for the drop in V_{oc} and efficiency for group 3.) A thickness of 2 μm has been selected as a conservative value for the fabrication of all future cells on this program.

3.6.3 Solar Cell Evaluation

3.6.3.1 Cell Parameters

We obtain the solar cell voltage-current characteristics via a quartz-iodine lamp, conventional electronic load and an x-y plotter. The quartz-iodine simulator is adjusted to AM1 equivalent with a calibrated standard silicon cell. Currently, we extract all photovoltaic data from the x-y plots, viz, Appendix 2, but separate meters will be added in the future to provide V_{oc}, I_{sc}, V_p and I_p directly. Four point Kelvin wiring, a vacuum chuck, and forced air cooling are basic features of the cell test fixture.

Dark measurements are made of the reverse current at v = -0.6 volts and v = -1.0 volts to obtain an estimate of the cell saturation current. The data (Section 4.3) give the total reverse currents at v = -0.6 volts, I_o'. The estimated value of the n-factor is obtained from the differential voltage for cell currents of 0.5 mA and 5.0 mA. This calculation assumes series resistance effects are negligible and that the cell characteristic can be represented by a single exponential expression. The result gives

$$n = (v_1 - v_2)/[(kT/q)\ln(I_1/I_2)] ,$$

which, for the usual conditions, reduces to $n = \Delta v/0.06$. Series resistance can be approximated from the slope of the voltage-current characteristic at high currents. The data tabulated in Section 4 use I = 180 mA and 200 mA and are not corrected for the effects of the n factor.

3.6.3.2 OCD Cell Lifetime Measurements

The lifetime measurement uses the open circuit voltage decay method.[7] The data are taken using a Tektronix 5 plug-in at a forward injection level of 1 mA/cm^2. The data obtained so far, Section 4, do not correlate with the short circuit-current or base lifetime; however, in some cases a correlation is obtained with the n-factor. Since the n-factor is a property of the junction, this measurement may provide a useful and convenient characterization of this important region of the device.

Thus, at this time the problem of directly measuring the base lifetime remains somewhat unresolved. Clearly, the short circuit current of the cell remains the most reliable and sensitive lifetime indicator. But to obtain an accurate numerical value for τ_B from I_{sc} requires making some rather fragile assumptions about the front and back surface losses. In any case, it is obvious that base lifetime and short-circuit must be closely correlated. As discussed earlier, we expect to obtain base lifetime by the photoconductive decay technique before and after processing. A complimentary method of making recombination lifetime on finished cell is thus desirable.

Should the OCD cell method prove unreliable, one potential alternative is a lateral mesa transistor test pattern which can be fabricated on wafers with our present cell processing sequence. This structure is similar to the single diffused transistor except that its current gain will be limited by both injection efficiency, due to high base doping, and by the base carrier transport factor. The common base current gain is given by:

$$\alpha = \alpha^* \gamma \ ,$$

where $\alpha^* = 1/(1 + W_B^2/2D_B\tau_B)$ is the base transport term and emitter injection factors:

$$\gamma = 1/(1 + (Q_B/D_B)/(Q_E/D_E)) \ .$$

The other quantities are defined as follows:

W_B is the base width.

D_B the base diffusion coefficient for electrons ($D_B = 35$).

Q_B the charge in the base is given by

$Q_B = N_A W_B$, where N_A is the base acceptor concentration.

τ_B is the base lifetime.

Q_E/D_E is a property of the emitter which is not well understood but which can be independently measured.

If we construct two transistor test structures with different basewidths, it should then be possible to determine the base lifetime. Test structures for this purpose are now being designed.

4. RESULTS

4.1 Ingot Evaluation

Baseline ingot growth has been completed and first generation ingot preparation and characterization are well underway. A summary of ingots prepared during the first quarter and their characteristics are shown in Table 4. Ingot identification is shown in Column 1. Column 2 identifies the trap impurity and the amount of dopant added to the melt. Seed and tang resistivity is given in the third column while the etch pit density is shown in the fourth column. The dislocation density is indicative of the slice taken from the seed region of the ingot.

Two impurity concentrations calculated for the seed region of the ingot are shown in the fifth column. The first concentration is obtained by calculating the impurity melt concentration from the weight of impurity added and multiplying by the equilibrium segregation coefficient. The second concentration shown is based on a melt concentration determined by analysis of the crucible remains. In general, agreement has been excellent with the exception of ingot W006-NI001. The melt analysis for this ingot indicated a significantly lower concentration than expected on the basis of impurity weight added to melt. This is attributed to dopant loss (the original high purity nickel sample was in powder form) from the crucible during melt-down. The lower impurity level in the ingot was subsequently confirmed by mass spectrographic analysis. The concentration of 1.7×10^{14} atoms/cm^3 is therefore indicative of the concentration in ingot W006-N1001.

Mass spectrographic analytical data is contained in column six. Subsequent reports will also include the results of neutron activation analysis as they become available. Although the results to date have been encouraging, more intensive analysis may be required to reduce the

Table 4. Summary of Baseline and First Generation Ingot Characteristics

1	2	3	4	5	6	7
Ingot ID	Trap Impurity/ Wt. (gms)	Seed ρ/Tang ρ (ohm-cm)	Dislocation Density (Etch Pits/cm^2)	Calculated Impurity* Conc. (1)/ Calculated Impurity Conc. (2) (Atoms/cm^3)	Mass Spec. Trap Conc. Atoms/cm^3	Comments
W-001-00-000	NA	3.2/2.8	DDF°	NA		Baseline/Process Standards
W-002-00-000	NA	4.0/2.9	DDF°	NA		Baseline/Process Standards
W-003-00-000	NA	3.6/3.1	DDF°	NA		Baseline/Process Standards
W-004-CR-001	CR/3.15	4.65/4.3	500	$1x10^{15}/0.82x10^{15}$	$1x10^{15}$	Poly Growth After 50% Pull
W-005-MN-001	MN/3.34	3.6/3.1	600	$1x10^{15}/0.82x10^{15}$	$2.5x10^{15}$	Poly Growth After 50% Pull
W-006-NI-001	NI/4.45	4.1/3.5	300	$1x10^{15}/0.17x10^{15}$+	$<3x10^{14}$	Routine
W-007-CU-001	CU/0.096	5.2/3.7	DDF	$1x10^{15}/1.18x10^{15}$	$1.5x10^{15}$	Routine
W-007-TI-001	TI/2.9	4.2/3.1	1800	$1x10^{15}/0.82x10^{15}$	Incomp.	Analysis in Progress
W-008-V-001	V/3.09	4.3/3.9	DDF	$1x10^{15}/1.19x10^{15}$	Incomp.	Analysis in Progress
C-1295	N/A	4.0-2.9		Audit Ingot	N/A	No Transition Elements Detected by Mass Spec.
C-1296	N/A	25		Audit Ingot	N/A	P.C. Decay Lifetime >20 Microseconds. No transition Elements Detected by Mass Spec.

* Calculated impurity concentration (1) based on weight of impurity added to the melt.
\+ Calculated impurity concentration (2) based on analysis of impurity concentration in crucible remains.
o Increase away from seed.

uncertainty level for concentrations determined by mass spectrographic analysis.

In addition to the first generation and baseline ingots, two crystals have been grown to audit the crystal puller for contamination. Ingot C-1289 was doped with boron to the same concentration as baseline material. This ingot was pulled following the growth of the chromium and manganese doped ingots. Mass spectrographic analysis detected no transition elements. Following copper doping, ingot C-1296 was pulled. A lower boron concentration was used in preparing ingot C-1296 to permit lifetime measurement using bulk RF photoconductive decay. The mass spectrographic analysis of this ingot was clean and the minority carrier lifetime was in excess of 20 microseconds. Slices from ingot C-1289 will be evaluated for cell performance and regular audit ingots will be prepared throughout the program or until adequate experimental evidence exists to conclude that contamination from run to run is not a problem.

4.2 Wafer Evaluation

4.2.1 Characteristics of Cr, Mn, Ni and Cu in Silicon

The type and kind of electrically active impurities in the doubly-doped silicon wafers will strongly influence the electrical properties and solar cell performance. Many of the impurity elements under study here have deep levels; form electrically active complexes with silicon, other dopants, or lattice defects; and can diffuse and precipitate from the lattice at relatively low temperatures. For this reason a discussion of the major characteristics of Cr, Mn, Ni and Cu, the first four impurities evaluated under the program, is an appropriate foundation for presentation of the experimental results described later.

Chromium

The solid solubility of Cr in silicon increases exponentially from 2.2×10^{13} cm^{-3} at 900°C to 2.5×10^{15} cm^{-3} at 1280°C.[8] Chromium diffuses interstitially with diffusivity $D = 0.01 \exp(-1.0\ eV/kT)$,

although the value of 1.0 eV for the activation energy would better fit a dissociative diffusion mechanism containing coupled elements of both interstitial and substitutional types.[9]

The supersaturated solid solution of chromium in silicon is unstable and decomposes at comparatively low temperature (∿200°C).[10] When the chromium concentration exceeds the acceptor concentration and the uncompensated chromium atoms can put electrons into the conduction band, the chromium atoms in solution are singly ionized during compensation and the carrier concentration in the silicon is very nearly intrinsic.

The existence of a Cr donor level at E_c -0.23 eV has been confirmed by several studies.[8,10,11] Donor levels at E_v +0.11 [10] and E_c -0.41 eV [12] have also been reported. However, some uncertainty exists about these two levels.

As might be expected from the solid solubility data, for one ohm-cm ($N_A = 1.6 \times 10^{16}$ cm^{-3}) or more heavily-doped p-type silicon, saturation by chromium does not change the conductivity type. Due to rapid precipitation at any reasonable cooling rate from the crystal growth diffusion or sintering temperatures, little chromium is available for compensation.

Manganese

The solubility of Mn in silicon varies from 10^{14} to 10^{16} cm^{-3} in the temperature range 1000-1350°C and is described by $N = 2.5 \times 10^{22} \exp(-2.10 \text{ eV/kT})$. A manganese rich surface layer (15-20 μm) has been noted on diffused samples, and is attributed to strong enrichment of the surface region with vacancies which bind manganese atoms to form low mobility complexes. Layers like these could be detrimental to solar cell performance and may necessitate development of compatible processing techniques.

Manganese migrates mainly by an interstitial mechanism in the form of Mn^+ ions. The diffusion coefficient for Mn in silicon varies from 1×10^{-6} to 2×10^{-5} cm^2/sec between 1000 and 1350°C range. The activation energy for diffusion is 1.3 eV.[13]

For Mn the distribution coefficient, k, is 10^{-5} which limits the amount of Mn that could be incorporated during crystal growth. Mn behaves as a donor and would convert initially p-type silicon to n-type. However, heating at about 300°C for 30 to 40 minutes precipitates most of the Mn.

Manganese reduces recombination lifetime and this effect is observable at the 10^{12} cm^{-3} concentration in silicon. Hall mobility and lifetime studies by the photoconductive decay method show the presence of electron traps.[14] Manganese introduces a single donor level at 0.53 eV from the conduction band.

Nickel

The solid solubility of nickel in silicon peaks around 10^{18} cm^{-3}.[15,16] The electrically active nickel concentration is, however, considerably lower than the solubility limit.[17] The diffusivity is given by $D = 0.10 \exp(-1.9/kT)$ and it is believed that diffusion proceeds by the interstitial mechanism.[18] Such rapid diffusivity combined with nickel's low solid solubility causes considerable precipitation during cooling from the diffusion or growth temperature, and most of the nickel becomes electrically inactive.[16,19] Due to its very small distribution coefficient ($<10^{-6}$) and the possible formation of six Ni-Si intermetallic compounds, it is difficult to introduce nickel in appreciable concentration into silicon during crystal growth from a melt.

Chua and Rose[20] found that nickel introduces two acceptor levels at 0.24 ± 0.01 eV and 0.37 ± 0.01 eV from the valence and conduction band edges respectively. Their results agree well with that of Tokumaru.[21]

Although deep levels are introduced by nickel, their effect on the minority carrier lifetime is poorly established. Lifetime in silicon has been improved considerably by plating the wafer surfaces with nickel prior to the heat treatment.[22] When nickel is diffused into silicon, the lifetime of devices is evidently improved rather than degraded.[22,23]

Due to its gettering action, nickel is considered an ineffective recombination center. Although relatively higher levels of Ni might be tolerated in the solar grade silicon, its incorporation into the crystal may be difficult without introducing precipitation.

Diodes fabricated with nickel-doped silicon exhibit a negative resistance region in their forward characteristics, and photoconductivity as a sublinear function of the illumination intensity.[24]

Copper

The maximum solid solubility of copper in silicon is 3×10^{18} cm^{-3} at 1300°C.[25] The diffusion coefficient, measured by the removal of layers of silicon containing radioactive copper, is given by $D = 0.04 \exp(-1.0/kT)$ in the temperature range 800-1100°C.[26] Higher diffusivities have also been measured.[27-29] Copper is believed to diffuse interstitially as a singly ionized species. This has been substantiated by diffusion experiments in an electric field.[30]

The energy levels of copper in silicon have been measured;[31-33] copper forms an acceptor level at E_v +0.49 eV and a donor level at E_v +0.23 eV. Some disagreement exists on the energy level (varies from 0.21 to 0.25 eV) for the donor center. Hall and Racette,[27] however, have shown an interstitial shallow donor in p-type and moderately doped n-type silicon. In heavier doped n-type the copper is in substitutional form -- possibly in a triple acceptor state.

Zibuts et al.[32] measured the hole capture cross-section for the neutral copper donor level to be 3.5×10^{-20} cm^2 and the photon capture cross-section for this level is 5×10^{-18} cm^2. These extremely low cross-sections are in disagreement with Leneke's[34] data which gives the hole cross-section as 2×10^{-14} cm^2. These values may be compared with the well known cross-section of 3×10^{-15} cm^2 for gold.

Copper precipitates at dislocations.[34,35] For this reason it is frequently used to decorate dislocations for microscopic examination.

Of the three impurities Cu, Ni and Fe, Cu exhibits the highest interaction energy for edge dislocations.[36] As such, diffusing Cu into the host Si lattice can increase the bulk lifetime in the material. Apparently, Cu atoms screen dislocations, making them less effective recombination centers. Cu deposited at dislocations loses its electrical activity. However, if the dislocation is torn away from the Cu shielding, e.g., by thermal quenching, both the dislocation and the remaining Cu become electrically active. In this case, the lifetime is reduced.[37,38] A decrease in lifetime with Cu was noted by Collins and Carlson.[31] Although Cu introduces deep energy levels into silicon, it probably is a poor recombination center due to precipitation.

4.2.2 Microstructure Evaluation

Sirtl etching wafers from the sliced ingots reveals a classic distribution of triangular etch pits on (111) surfaces, Fig. 10. The etch pit densities for the ID-sawed, chem-polished wafers, Table 5, is consistent with the values obtained on the bulk ingots, Table 4. (111) topographs run on the unprocessed wafers, Fig. 11, also confirm their relatively low dislocation contents prior to diffusion, and illustrate that the defect density rises toward the wafer edge. This perhaps indicates that some surface damage was introduced during ingot grinding although even at the wafer edge EPD is $< 10^4$ cm^{-2}.

Table 5

Etch Pit Densities on
Baseline and Transition Metal Doped Wafers

Ingot Number	Location	Etch Pit Density (no./cm^2)
W003 (baseline)	--	964
W004 Cr		560
W005 Mn		450
W006 Ni		<100
W007 Cu		0

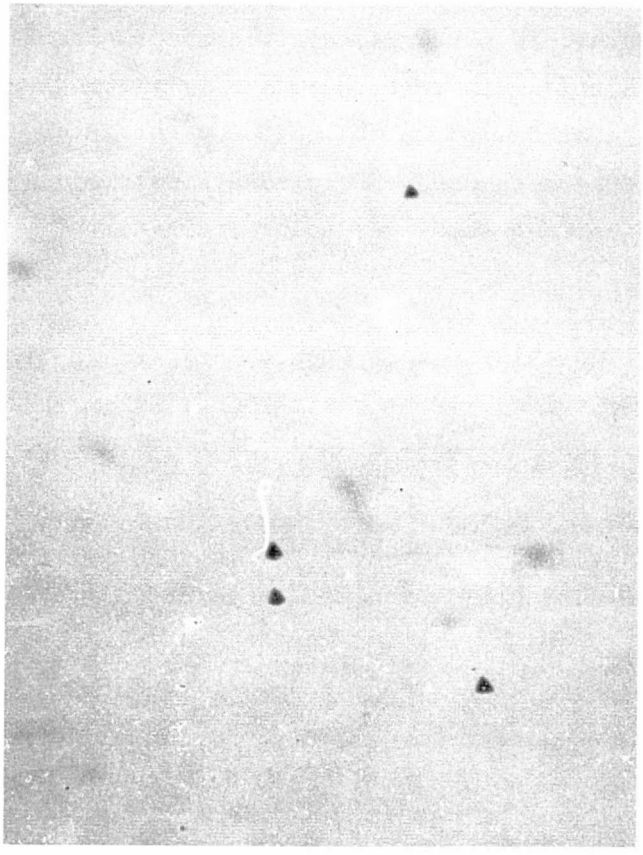

Fig. 10. Dislocation etch pits on baseline wafer (W003); Sirtl etched 5 minutes.

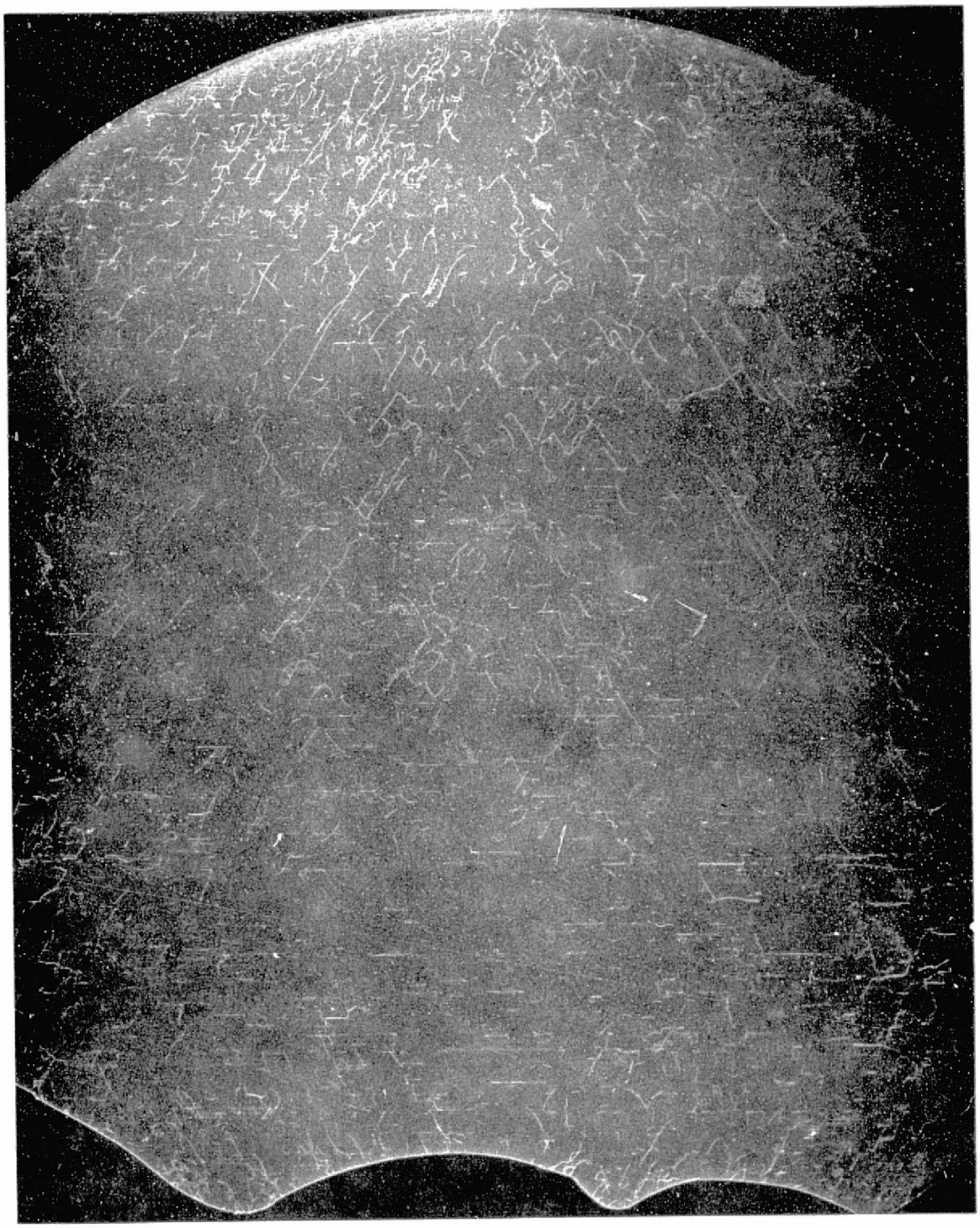

Figure 11

While short-etch time experiments would be beneficial for assessing microprecipitation in the wafers, we have deferred such experiments until suitable samples are identified by electrical or device measurements.

4.2.3 Spreading Resistance Measurements

The impurity profiles, N/N_{avg} vs wafer radius, obtained via spreading resistance measurements (Appendix 1) illustrate that, with the exception of the Mn-doped ingots, the transition metal doped material is comparable in homogeneity to the baseline material. The net average acceptor concentration and standard deviations of the profiles are tabulated below:

Table 6

Radial Resistivity Variations on Baseline and Transition Metal Doped Ingots

Ingot No.	Wafer Location	Net Average Acceptor Concentration cm^{-3}	Fractional Standard Deviation of Net Acceptor Doping
W001	--	4.3×10^{15}	3.238×10^{-2}
W002	--	3.9×10^{15}	4.565×10^{-2}
W003	--	4.5×10^{15}	5.976×10^{-2}
W004 Cr	seed	3.1×10^{15}	3.663×10^{-2}
	tang	3.1×10^{15}	2.472×10^{-2}
W005 Mn	seed	2.7×10^{15}	10.390×10^{-2}
	tang	2.8×10^{15}	7.139×10^{-2}
W006 Ni	seed	3.8×10^{15}	2.805×10^{-2}
	tang	4.2×10^{15}	4.338×10^{-2}
W007 Cu	seed	4.0×10^{15}	2.934×10^{-2}
	tang	4.4×10^{15}	2.439×10^{-2}

Although some short range variation in the profiles appears, Appendix 1, it is difficult to ascribe this to the influence of the transition metals per se. Since Mn is known to produce donor levels in silicon, it's possible that some compensation occurs in that ingot due to Mn segregation during crystal growth.

4.2.4 Wafer Lifetime Measurements

4.2.4.1 Recombination Lifetime

Specimens prepared on W002 baseline material processed through diffusion exhibit typical oscilloscope responses like that in Fig. 12. The diffused layers were removed by etching prior to the measurement. The vertical axis is proportional to resistivity since the sample voltage is applied to the oscilloscope terminals under constant current conditions. The effective or measured recombination lifetime, τ_r', is obtained by finding the time required for the incremental conductivity to fall to one half the initial value and dividing it by ℓn 2 (0.693). The effective lifetime, τ_r', measured for this sample is 1.44 μsec. The incremental photovoltage change to dark voltage, $\Delta v/v$, was 1.379×10^{-3}, and the mobility ratio of holes to electrons, b = 0.38. The injection ratio defined by Eq. (4), Section 2, is therefore 7.615×10^{-4}, well within low level injection range.

The majority carrier density for W002 is 8.87×10^{15} cm^{-3}, and the peak excess minority carrier density generated by the LED is 6.75×10^{12} cm^{-3}, assuming a uniform distribution throughout the thickness of the sample. The distribution is, however, known to be nonuniform with a change of 1/e for every 40 μm into the sample. The lifetime, τ_r', after etching the sample for 7 minutes remained at 1.44 μsec. Corrections for surface recombination have not yet been completed and no value is presently available for τ_r.

4.2.4.2 Generation Lifetime

A typical capacitance-time plot obtained while measuring sample W002 is illustrated in Fig. 13. The oxide thickness for the MOS device,

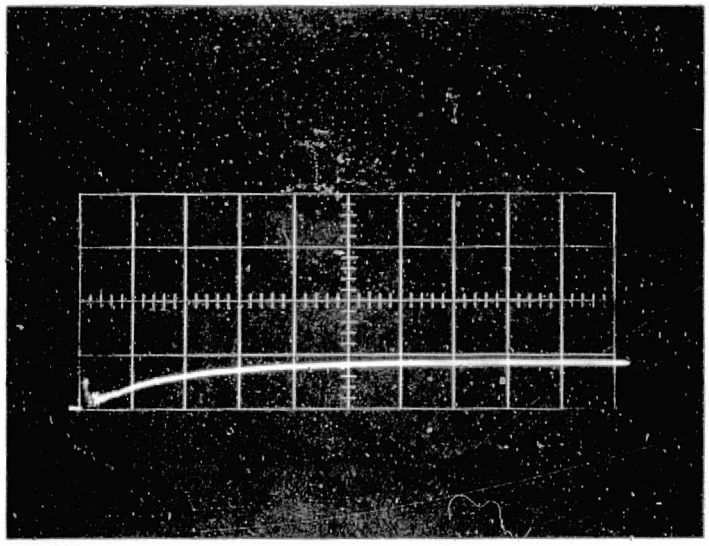

Fig. 12. PDL oscilloscope recording for diffused, unetched W002 baseline wafer. I_t = 10 mA, I_T = 0, $\Delta V/V$ = .004/2.9.

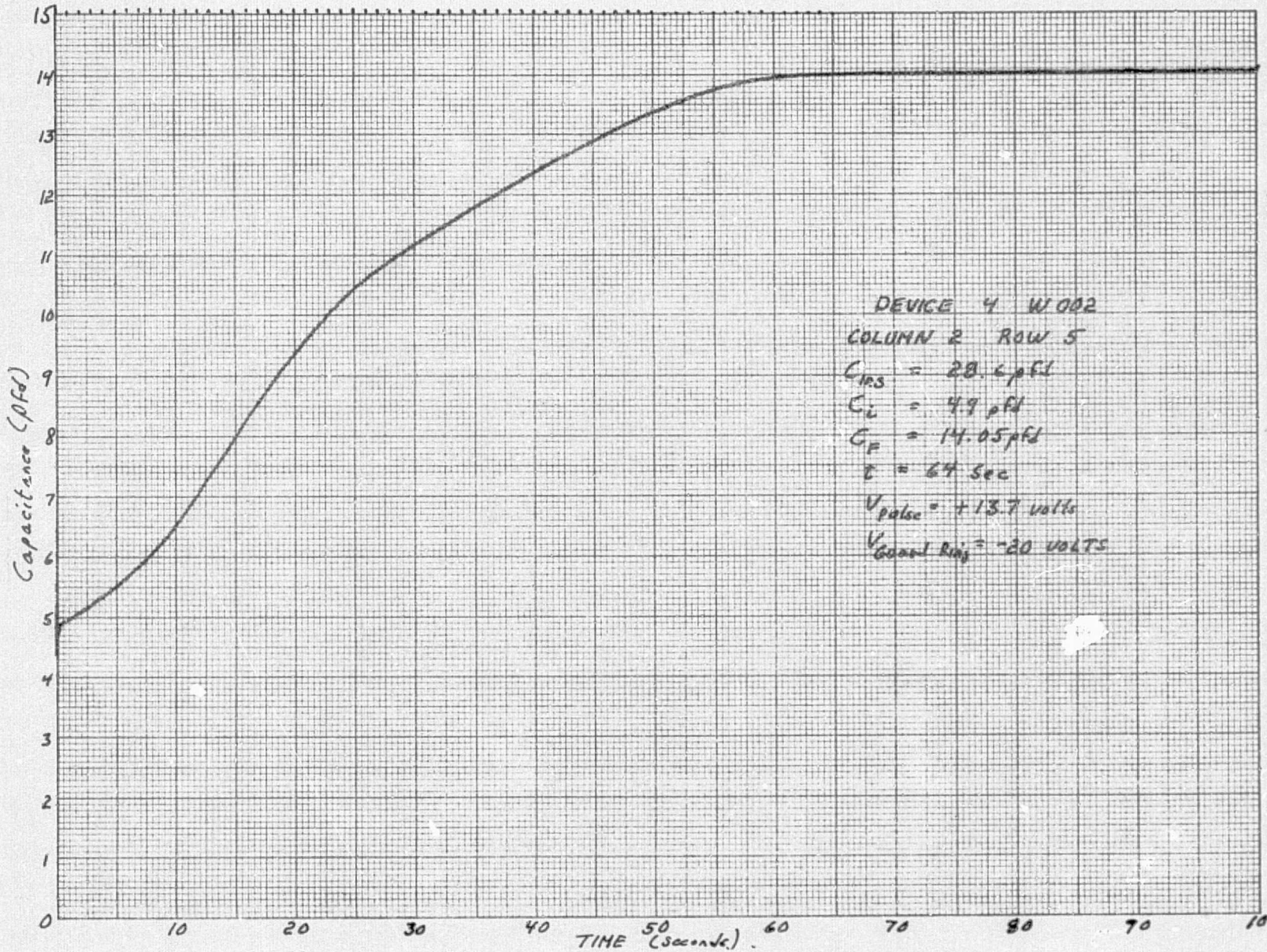

Fig. 13. Capacitance-time recovery plot after deep depletion of MOS Device No. 4.

W_{ox}, was calculated from

$$W_{ox} = \frac{K_{ox} \varepsilon_o A}{C_{ins}} \tag{5}$$

and the acceptor concentration was determined from C_F/C_{ins}. The data from the curves were manually digitized and curve fitted by a computer routine. The computer program corrects for errors made in digitizing, then calculates the value of d/dt $(C_{ins}/C)^2$ and $(C_F/C - 1)$ for every increment of time selected in the digitizing step. From the data a Zerbst[39] plot of d/dt $(C_{ins}/C)^2$ vs $(C_F/C - 1)$ is constructed, Fig. 14. The effective generation lifetime, τ_g^*, is then calculated from Eq. (6).

$$\tau_g^* = 2 \frac{n_i}{N_D} \frac{C_{ins}}{C_F} \times \frac{d[C_F/C-1]}{d[-d/dt(C_{ins}/C)^2]} \tag{6}$$

The reciprocal slope of Fig. 14 is equal to the last term in the equation. The generation lifetime, τ_g^*, for W002 is equal to 55.6 μsec.

The surface generation velocity for a depleted surface, S_o, is given by Schroder's[40] Eq. (7) evaluated at t = 0

$$s_o = \frac{N_D}{n_i} \frac{K_s}{K_{ox}} W_{ox} \frac{C_{ins}^2}{C^3} \frac{dC}{dt} - \frac{K_s}{K_{ox}} \frac{C_{ins}}{C} W_{ox} (1-C/C_F)/\tau_g^* \Bigg|_{\text{at } t=0} \tag{7}$$

The value of S_o determined for this sample is -0.230 cm/sec, the negative sign indicating that the value is less than the error in digitizing the data. Normally S_o ranged from 0.215 to 0.67 cm/sec. The actual bulk generation lifetime, τ_g, can now be calculated from Eq. (8)

$$\tau_g = \tau_g^*/(1 - 2S_o \tau_g^*/r) \tag{8}$$

where r is the radius of the metal gate (1.693×10^{-2} cm).

The results obtained using Eqs. (5), (6), and (8) are presented in Table 7 for the test structures fabricated on virgin baseline wafers.

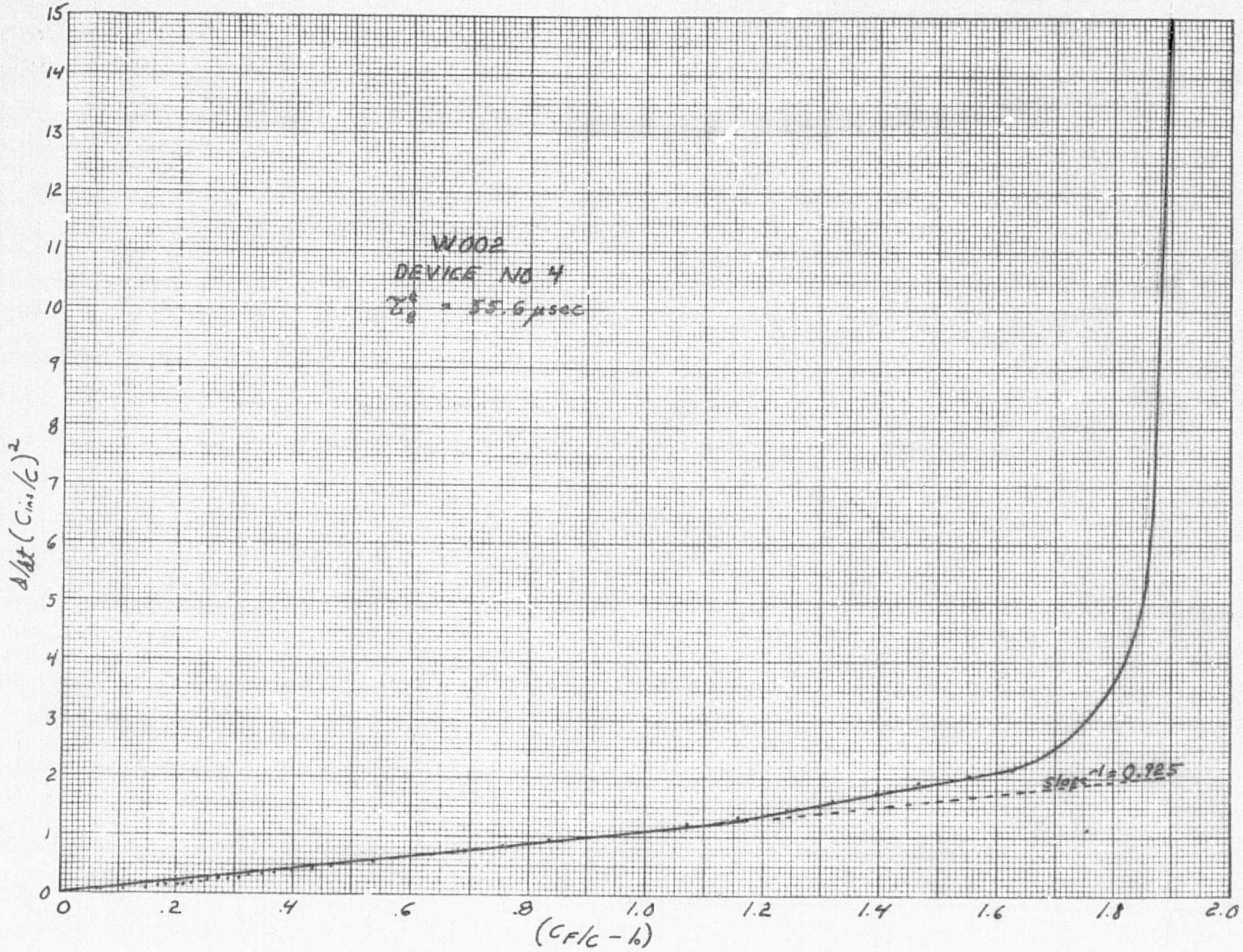

Fig. 14. Zerbst plot of C-t data shown in Fig. 5.

Table 7

Summary of Pulsed MOS Measurements

Baseline Lot	Sample No. (Position No.)	W_{ox} (A°)	N_a (cm^{-3})	τ_g* from Eq. (9) (μsec)	τ_g* From Zerbst Plot (μsec)	τ_g (μsec)
W001	1 (2-3)	1217	9×10^{15}	38.24	759	807.4
W001	2 (2-5)	1262	8.5×10^{15}	3.02	130	†
W001	none (2-4)	1198	8.8×10^{15}	21.7	--	--
W001	none (3-4)	1153	1.2×10^{16}	2.1	--	--
W001	none (4-3)	1184	9.2×10^{15}	30.2	--	--
W001	none (4-6)	1188	9.8×10^{15}	21.5	--	--
W001	none (4-7)	1170	6.6×10^{15}	16.5	--	--
W002	3 (1-3)	1071	7.8×10^{15}	14.2	69.3	†
W002	none (2-3)	1126	1×10^{16}	15.5	--	--
W002	4 (2-5)	1059	8.8×10^{15}	6.7	55.6	55.6
W003	none (2-4)	1102	8.5×10^{15}	18.3	--	--
W003	5 (3-4)	1094	9.1×10^{15}	30.2	657	†

†Calculations are invalid due to presence of negative terms.

The value of τ_g* given in column 5 of the table was determined by the approximation in Eq. (9),

$$\tau_g^* = \frac{n_i C_F}{8 N_a C_{ins}} \left(1 + \frac{C_i}{C_F}\right)^2 t \qquad (9)$$

in which t is the time required for the capacitance to reach the terminal value C_F. The data in column 5, Table 7, were previously reported as preliminary results pending computer evaluation. It is readily apparent that the approximation method fails for this particular case.

It is also evident that the procedure involved in determining the generation lifetime, τ_g, is lengthy; thus, only five structures were

evaluated in these tests. For this reason, and because the technique measures the generation lifetime, τ_g, rather than recombination lifetime, τ_r, no major effort will be expended on these measurements in the future.

4.3 Solar Cell Testing

Data for the cells fabricated from the first four doubly-doped ingots, Table 8, indicate that chromium and manganese produce the largest effect on solar cell performance while copper and nickel degrade the cells only little. The I-V curves from which the table was constructed constitute Appendix 2. Cell efficiencies are depressed about 28% by chromium, 23% by manganese, 3% by nickel and only 1% by copper relative to solar cells processed concurrently on baseline (standard) wafers. The junction properties, fill factors and n exhibit insignificant changes.

The reduction in cell efficiencies for the chromium and manganese-doped devices were perhaps to be expected, viz. Section 4.2. The chromium-doped cell, however, also displays considerable variation in performance as well as higher than usual series resistance. The latter observation suggests possible processing problems and this set will be rerun if further experiments verify this implication. The remaining runs provided well-grouped data.

As we noted earlier, the minimal effect of nickel on device parameters is anticipated by published results showing that nickel exhibits gettering properties. The behavior of copper, however, is somewhat surprising. The performance of the copper-doped devices is virtually identical to cells fabricated at the same time from the baseline material, Table 8 and Appendix 2. Two alternative explanations for this apparently anomalous result are (1) copper has completely precipitated from the silicon lattice and the precipitates are ineffective recombination centers, or (2) most of the copper was gettered from the lattice during the phosphorous diffusion treatment. The latter possibility seems more likely.

Although the experimental data, Table 8, are as yet limited, there are some general observations which may be drawn about metal

Table 8

Photovoltaic Characteristics of Transition Metal Doped Solar Cells

Run	Dopant/Conc.	V_{OC} mV	I_{SC} mA	Efficiency %	Fill Factor %	I_o' µA	n	R_S Ω	τ_{OCD} µS
60105 Standard		555	22.25	9.55	76	.7	1.3	2.5	5.6
60105-1C	CR 1×10^{15}	525	17.5	6.69	73	1.65	1.33	5	5
-2C		530	17.6	6.97	75	1.12	1.33	4.8	6.25
-3C		520	15	5.23	67	.94	1.33	2	3
-4C		535	18.5	7.29	74	9.24	1.33	2	5.5
-5C		510	16.0	5.91	62	1.06	1.67	3	4.25
-6C		535	19.0	7.59	75	20.26	2.33	1	6.25
-1E		535	18	7.21	85	12.1	1.33	2.5	5
-2E		535	18.7	7.21	72	11.18	1.68	1	3.75
-3E		535	18.7	7.48	75	9.42	1.68	4	3.25
60108 Standard		550	22.5	9.7	79	3.08	1.3	.6	5.6
60108-1C	Mn 1×10^{15}	523	17.75	7.21	78	1.40	1.17	.5	5.2
-2C		515	17.0	6.57	75	2.73	1.33	.5	1.95
-3C		520	17.5	6.98	77	1.90	1.17	1.0	3.25
-4C		520	17.5	6.98	77	5.81	1.50	.5	3.9
-5C		520	17.5	6.98	77	3.64	1.33	.5	5.2
-1E		516	16.75	6.60	76	1.49	1.33	1	3.9
-2E		516	17.35	6.91	77	4.96	1.17	1.5	3.25
-3E		516	16.75	6.72	78	5.13	1.33	1	3.25
-4E		516	17.20	6.79	77	.98	1.33	1	1.95

Table 8 (Con't)

Run	Dopant/Conc.	V_{oc} mV	I_{SC} mA	Efficiency %	Fill Factor %	I_o' μA	n	R_S Ω	τ_{OCD} μS
60114 Standard		550	22.75	9.60	77	3.00	1.3	1	
60114-1C	Ni 2×10^{14}	535	21.65	8.55	74	1.37	1.50	.5	
-2C		539	21.65	8.99	77	1.37	1.17	3.5	
-3C		539	21.65	8.8	75	1.28	1.33	2	
-4C		539	21.65	8.99	77	.31	1.17	3	
-5C		539	21.65	8.8	75	.41	1.50	2	
-6C		535	21.65	8.55	74	2.04	1.67	3	
-1E		545	22.7	9.45	76	1.81	1.17	2	
-2E		545	22.5	9.21	75	1.86	1.5	1	
-3E		540	22.5	9.21	76	.24	1.17	.5	
-4E		545	22.5	9.17	75	.72	1.30	1	
-5E		540	22.4	9.06	75	1.25	1.50	3	
-6E		545	22.5	9.18	75	11.96	1.18	1	
-7E		535	22.0	9.02	76	13.54	1.50	1	
-8E		545	22.5	9.17	75	1.24	1.50	4	
60120 Standard		550	22.75	9.78	78	1.1	1.17	.7	
60120-1C	Cu 1×10^{15}	550	22.5	9.77	79	7.38	1.5	.5	
-2C		550	22.6	9.61	77	2.28	1.5	.5	
-3C		550	22.6	9.61	77	.55	1.17	.5	
-4C		545	22.5	9.37	76	5.67	1.83	1	
-5C		545	22.4	9.55	78	9.19	1.83	.5	
-6C		545	22.5	9.29	76	8.61	1.33	1	
-1E		545	22.5	9.43	77	1.59	1.5	.5	
-2E		545	22.4	9.41	77	6.39	1.83	1	
-3E		550	22.5	9.65	78	.34	1.17	1	
-4E		546	22.5	9.43	77	.62	1.33	2	
-5E		547	22.5	9.43	77	3.30	1.67	1	
-6E		542	21.75	9.00	76	6.22	1.67	1	

contaminants in silicon crystals. The solubilities for most metal impurities are several orders of magnitude smaller at room temperature than at the growth temperature for an ingot doped to the 10^{15} cm^{-3} level. It is therefore likely that most of the metal is present as a precipitate. The performance degradation observed with chromium and manganese may not be associated with the precipitates themselves but with the very much smaller numbers of these atoms remaining on lattice sites or at isolated interstitial locations. In turn, this implies that degradation produced by chromium or manganese would be essentially unchanged with doping levels reduced even by several orders of magnitude. An independent study of lifetime in manganese-doped silicon by Carlson[14] is in general agreement with this conclusion. Future data should provide verification of this hypothesis, and specific experiments are planned for this purpose.

5. PROGRAM STATUS

5.1 Present Status

As depicted in Fig. 15, all elements of the program are on schedule.

During this quarter we have:

- completed growth of the boron-doped baseline ingots,
- completed growth of six doubly-doped first generation ingots (B + Cr, Mn, Ni, Cu, Ti and V)
- completed the chemical analysis of the Cr, Mn, Ni and Cu-doped ingots
- completed the microstructural and electrical evaluation of the baseline material
- completed design and test of the solar cell masks
- established a standardized solar cell fabrication sequence and produced baseline cells with typical efficiencies of 11-13% (AM1),
- set-up and tested equipment for lifetime measurements
- fabricated and tested solar cells on Cr, Mn, Ni and Cu-doped material.

5.2 Future Activity

During the next quarter:

- growth, chemical analysis, evaluation and solar cell testing of all first generation doubly-doped ingots will be completed;
- growth, analysis and solar cell testing of most second generation ingots will be completed;
- growth and chemical analysis of the third generation crystals will be initiated;

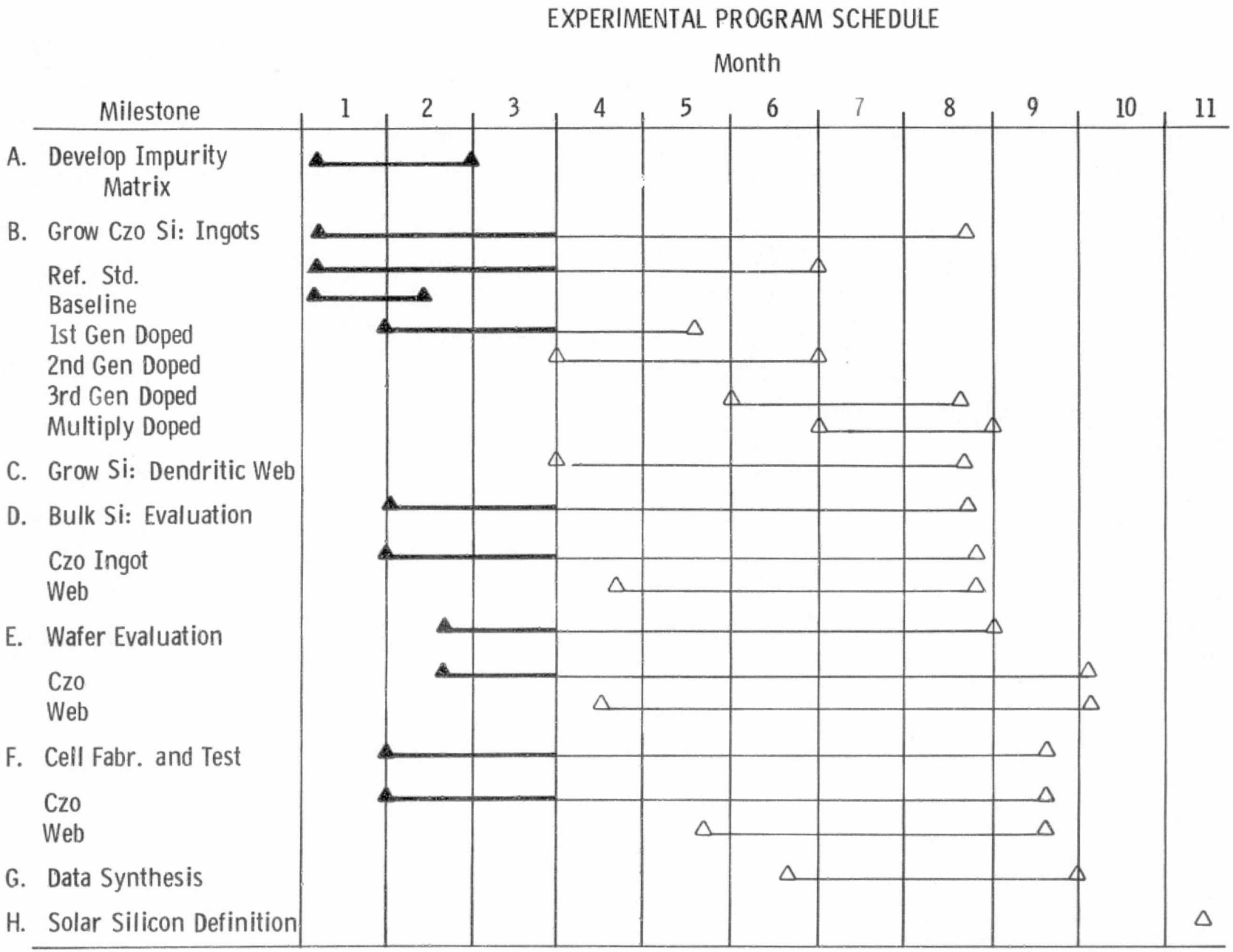
EXPERIMENTAL PROGRAM SCHEDULE
Month
Milestone
1
2
3
4
5
6
7
8
9
10
11
A. Develop Impurity Matrix
B. Grow Czo Si: Ingots
Ref. Std.
Baseline
1st Gen Doped
2nd Gen Doped
3rd Gen Doped
Multiply Doped
C. Grow Si: Dendritic Web
D. Bulk Si: Evaluation
Czo Ingot
Web
E. Wafer Evaluation
Czo
Web
F. Cell Fabr. and Test
Czo
Web
G. Data Synthesis
H. Solar Silicon Definition

Figure 15

- synthesis of microstructural, chemical, electrical and solar cell data for the evaluation of impurity effects on cell performance and feedback to multiply-doped crystal growth will be initiated;
- growth and evaluation of doped-web crystals will be underway.

6. REFERENCES

1. D. Stevenson and R. Keyes, "Measurement of Carrier Lifetimes in Germanium and Silicon," J. Appl. Phys. 26, 2 (1955).

2. K. Graff, H. Pieper, G. Goldback, "Carrier Lifetime Doping of P-Type Silicon by Annealing Processes," Semiconductor Silicon/1973, eidted by Juff and Burgess, Electrochem. Soc., 111 (1973).

3. W. R. Runyan, Silicon Semiconductor Technology, McGraw-Hill, 187 (1965).

4. E. Tannenbaum, "Detailed Analysis of Thin Phosphorus-Diffused Layers in P-Type Silicon," Sold-St. Electron. 2, 123 (1961).

5. J. C. Irvin, "Resistivity of Bulk Silicon and of Diffused Layers in Silicon," B.S.T.J. 41, 387 (1962).

6. H. Fischer, J. R. Gereth, New Aspects for the Choice of Contact Metals for Silicon Solar Cells, IEEE Conference Record of the Seventh Photovoltaic Specialists Conference (1968).

7. S. R. Lederhandler and L. J. Giacoletto, "Measurements of Minority Carrier Lifetime and Surface Effects in Junction Devices," Proc. IRE 43, 477-483 (April 1955).

8. W. Wurken, K. Roy and J. Hesse, Mat. Res. Bulletin 9, 971 (1974).

9. D. L. Kendall and D. B. deVries, "Semiconductor Silicon," 1969, edited by R. R. Haberecht and E. L. Kern, Electrochemical Society.

10. A. A. Zolotukhin and L. S. Milevskii, Soviet Phys. - Solid State 13, 1598 (1972).

11. H. H. Woodbury and G. W. Ludwig, Phys. Rev. 117, 102 (1960).

12. A. A. Lebedev and N. A. Sultanov, Soviet Phys. - Semiconductors 4, 1900 (1971).

13. M. K. Bakahdyrkhanov, B. I. Boltaks, and G. S. Kulikov, Soviet Phys. - Solid State 14, 1441 (1972).

14. R. O. Carlson, Phys. Rev. 104, 937 (1956).

15. Aalberts and M. L. Verheijke, Appl. Phys. Lett. 1, 19 (1962).

16. M. Yoshida and K. Furusho, Jap. J. Appl. Phys. 3, 521 (1964).

17. M. Yoshida and K. Saito, Rev. Electr. Commun. Lab. 16, 92 (1968).

18. H. P. Bonzel, Phys. Stat. Sol. 20, 493 (1967).

19. W. J. Shattes and H. A. R. Wegener, J. Appl. Phys. 29, 866 (1958).

20. W. B. Chua and K. Rose, J. Appl. Phys. 41, 2644 (1970).

21. Y. Tokumaru, Jap. J. Appl. Phys. 2, 542 (1963).

22. S. J. Silverman and J. B. Singleton, J. Electrochem. Soc. 105, 591 (1958).

23. J. E. Lawrence, Trans. Met. Soc. AIME 242, 484 (1968).

24. A. A. Lebedev, A. T. Mamadelimov and N. A. Sultanov, Soviet Phys. - Semiconductors 5, 1990 (1972).

25. F. A. Trumbore, B.S.T.J. 39, 205 (1960).

26. B. I. Boltaks and I. I. Sosinov, Sov. Phys. - Tech. Phys. 3, 636 (1958).

27. R. N. Hall and J. H. Racette, J. Appl. Phys. 35, 379 (1964).

28. J. D. Struthers, J. Appl. Phys. 27, 1560 (1956).

29. C. S. Fuller, J. D. Struthers, J. A. Ditzenberger and K. B. Wolfstirn, Phys. Rev. 93, 1182 (1954).

30. C. J. Gallagher, J. Phys. Chem. Solids 3, 82 (1957).

31. C. B. Collins and R. O. Carlson, Phys. Rev. 108, 1409 (1957).

32. Yu. A. Zibuts, L. G. Paritskii, S. M. Ryvkin and Zh. G. Dokholyan, Sov. Phys. - Solid State 8 (1967).

33. H. Irmler, Z. Naturforsch. 13a, 557 (1958).

34. H. Lemke, Phys. Stat. Sol. (a)1, 283 (1970)

35. J. E. Lawrence, J. Electrochem. Soc. 112 (1965).

36. J. E. Lawrence, Trans. Met. Soc. AIME 242, 484 (1968).

37. L. S. Milevskii, Sov. Phys. - Solid State 4, 311 (1962).

38. L. S. Milevskii, Sov. Phys. - Solid State 2, 1980 (1960).

39. M. Zerbst, "Relaxationseffekte an Halbleiter-Isolator-Grenzflachen," (Relaxation Effects at Semiconductor-Insulator Interfaces), Z. Angew. Phys. 22, 30-31 (1966).

40. D. K. Schroder and J. Guldberg, "Interpretation of Surface and Bulk Effects Using the Pulsed MIS Capacitor," Solid State Elect. 14, 1285 (1971).

7. APPENDIX

7.1 Appendix 1 -- Spreading Resistance Profiles for Transition Metal Doped Wafers

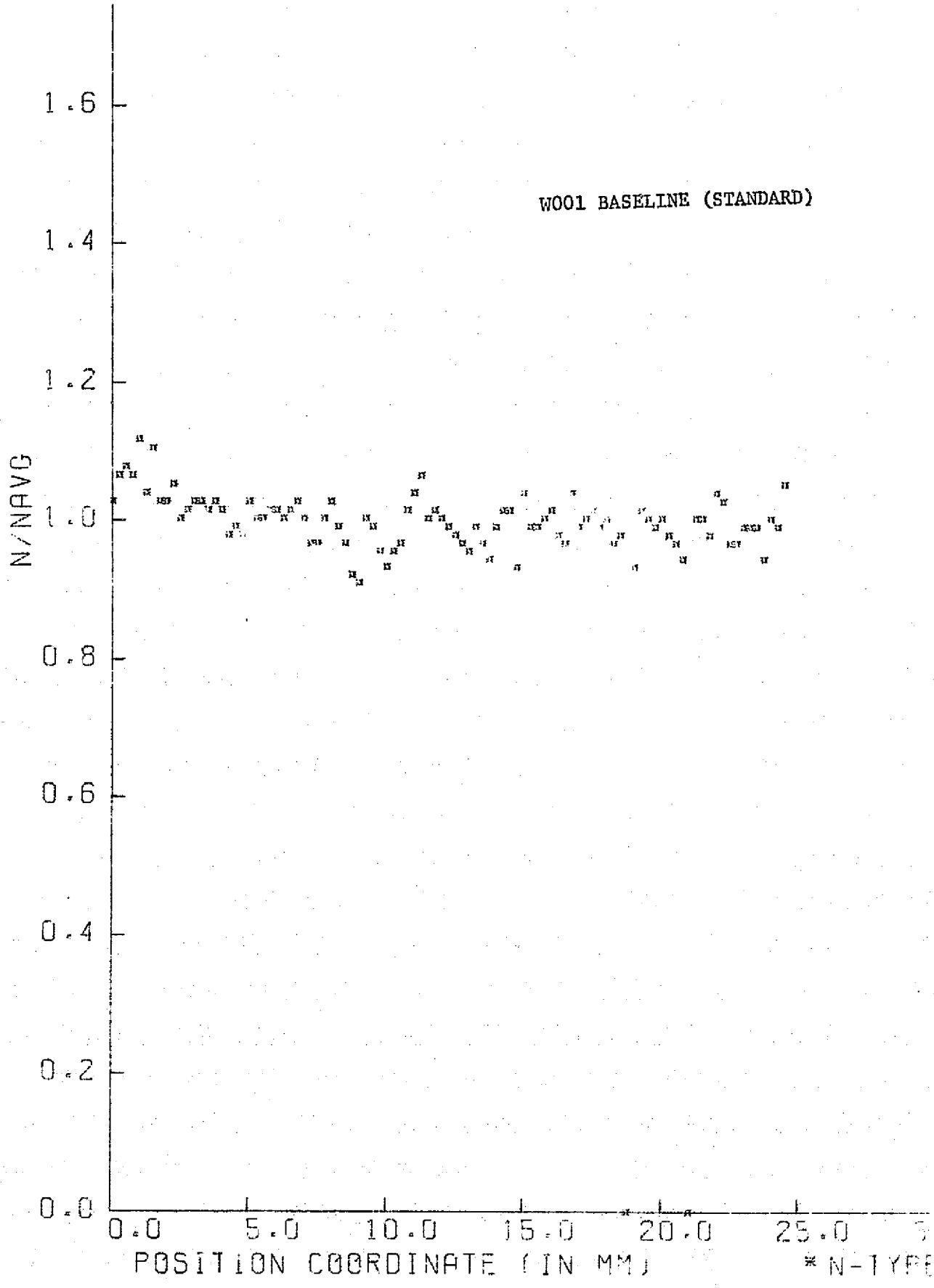

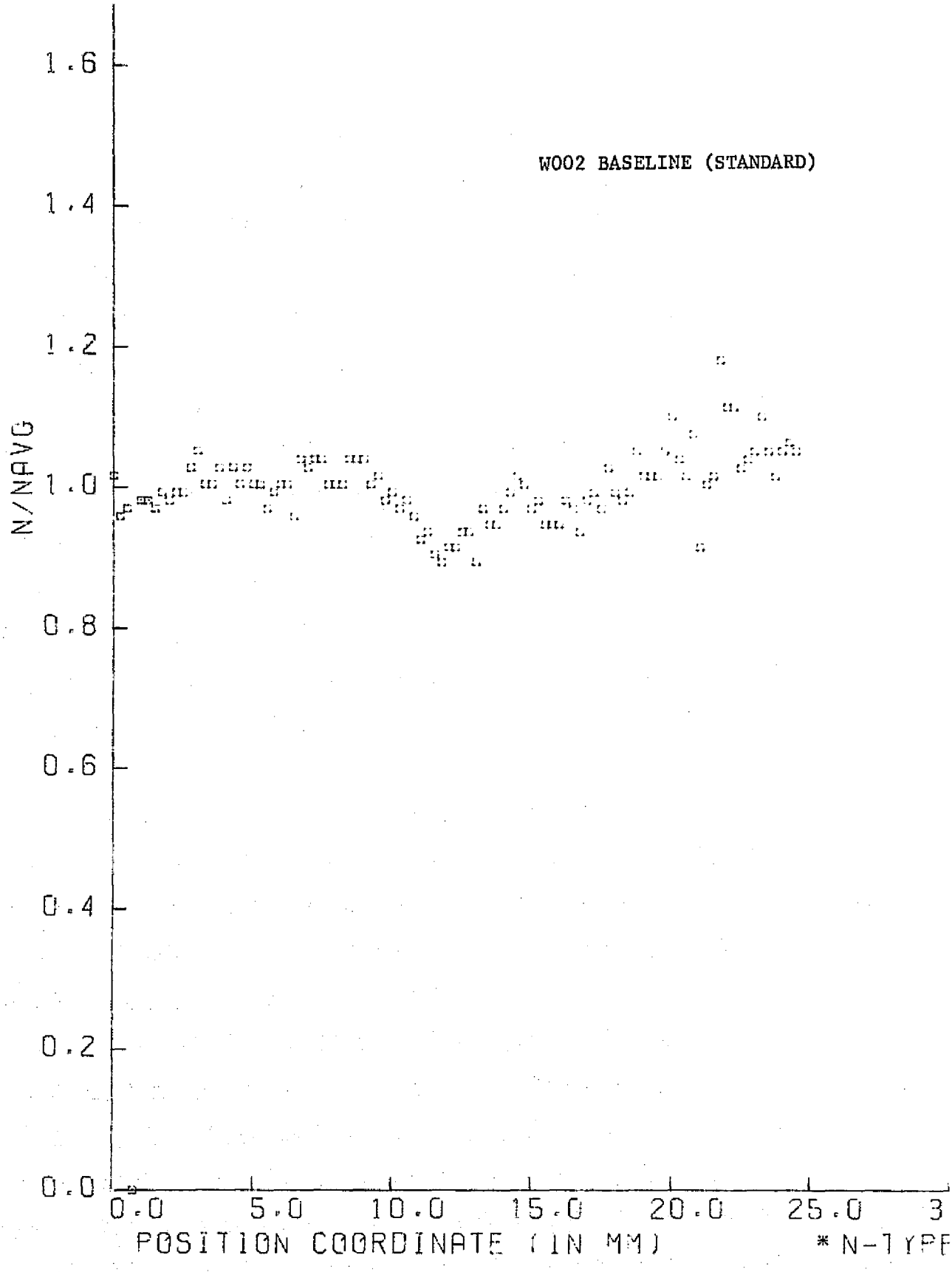
W002 BASELINE (STANDARD)
N/NAVG
1.6
1.4
1.2
1.0
0.8
0.6
0.4
0.2
0.0
0.0
5.0
10.0
15.0
20.0
25.0
3
POSITION COORDINATE (IN MM)
* N-TYPE

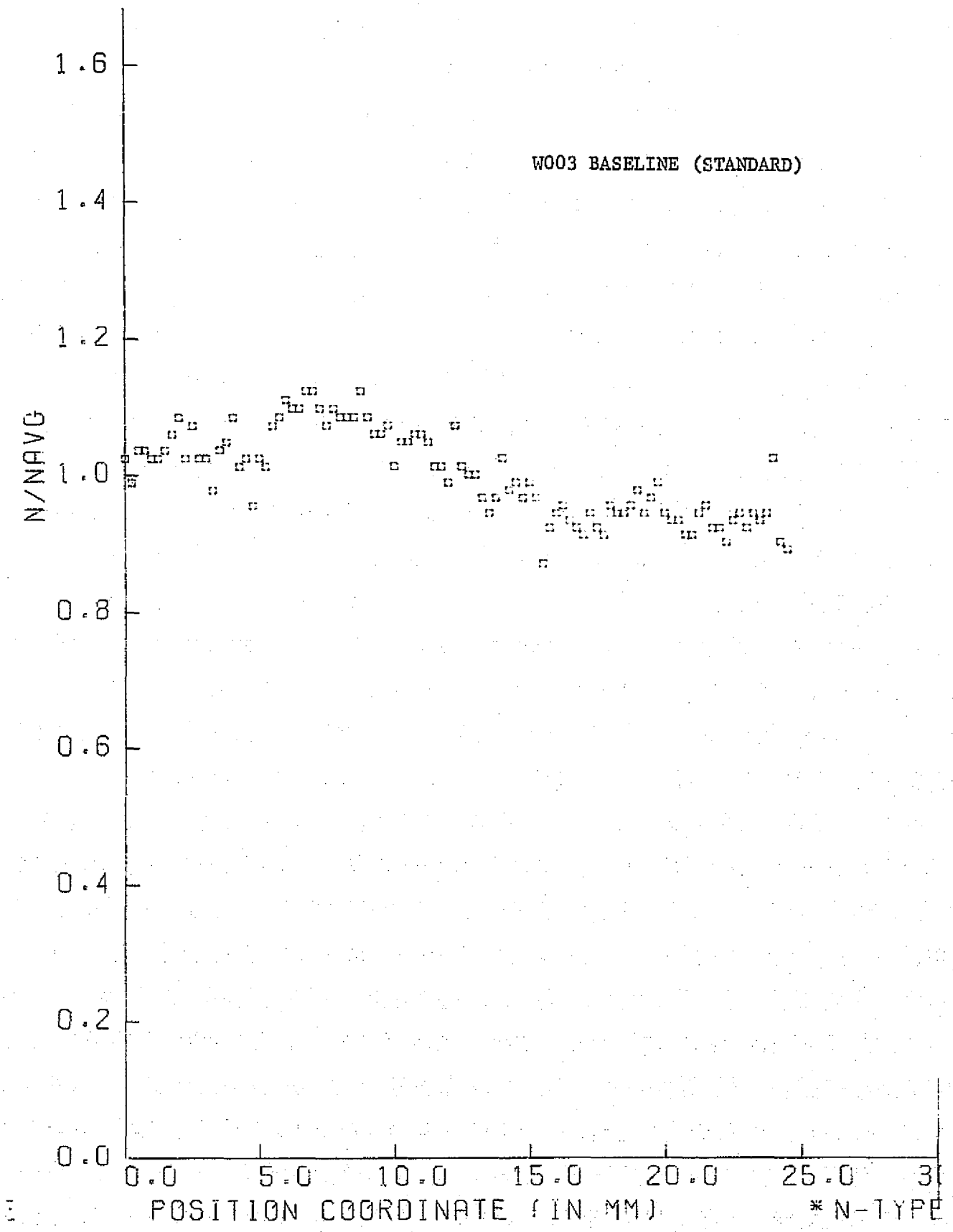
W003 BASELINE (STANDARD)
N/NAVG
1.6
1.4
1.2
1.0
0.8
0.6
0.4
0.2
0.0
0.0
5.0
10.0
15.0
20.0
25.0
POSITION COORDINATE (IN MM)
*N-TYPE

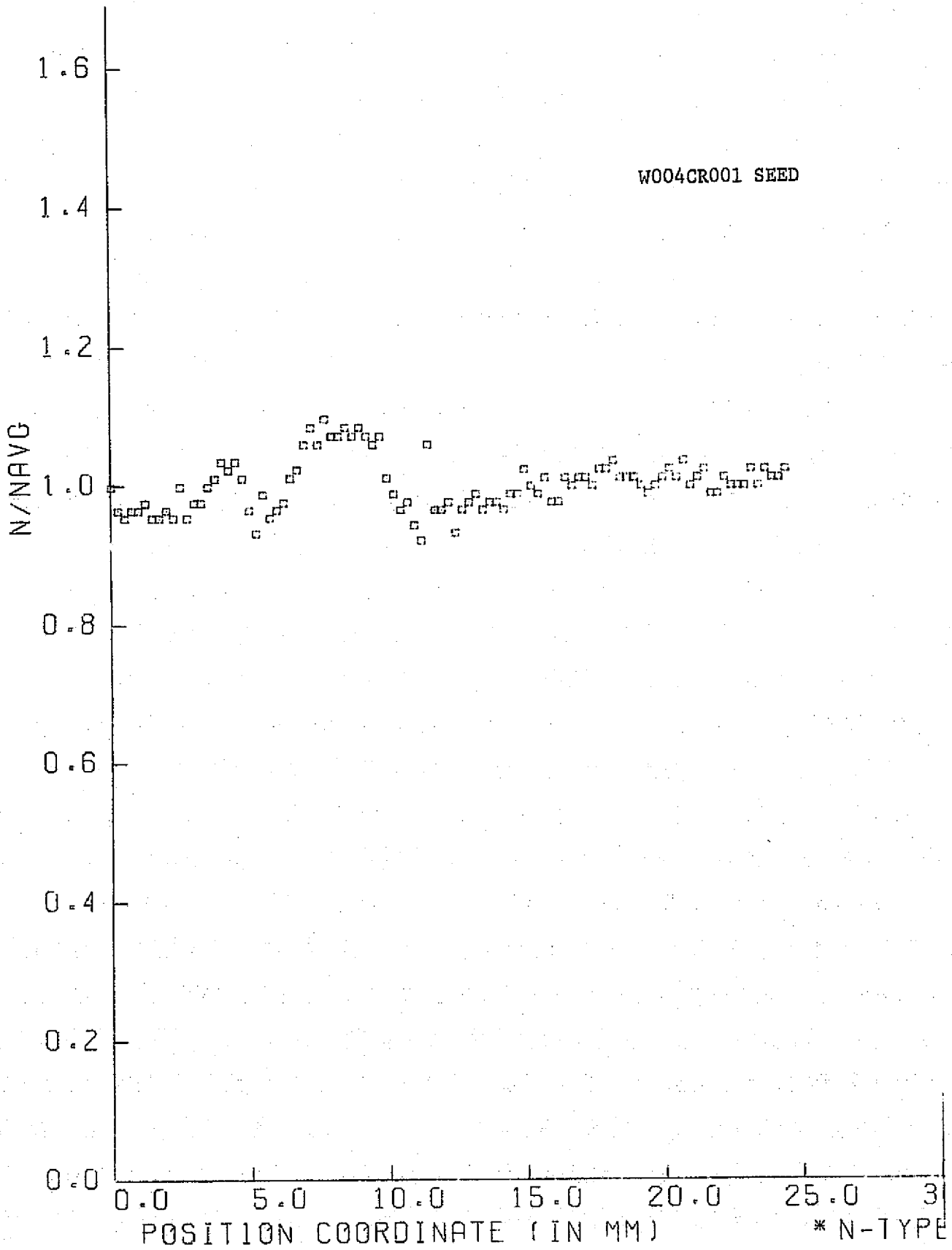

ORIGINAL PAGE IS
OF POOR QUALITY

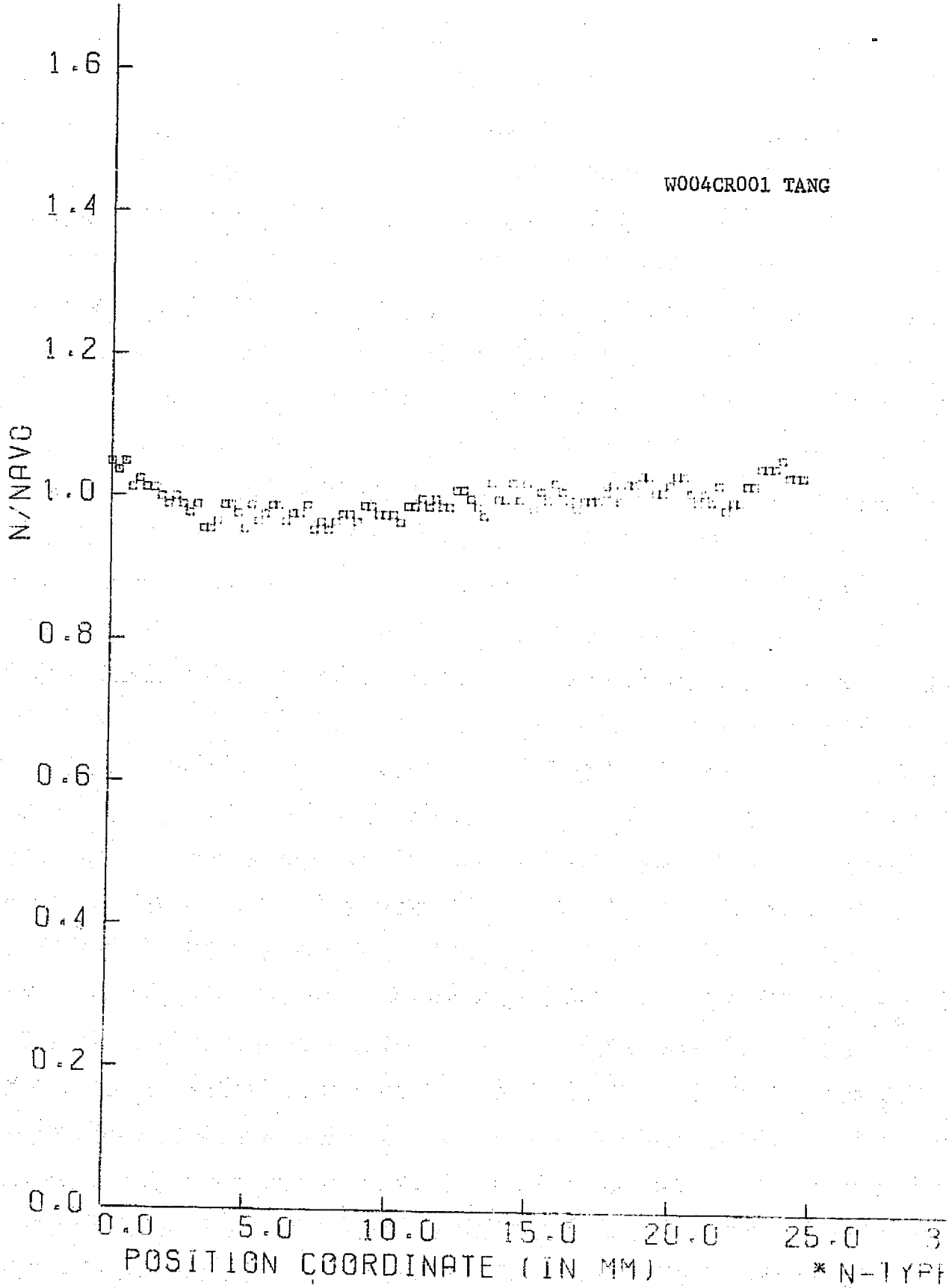

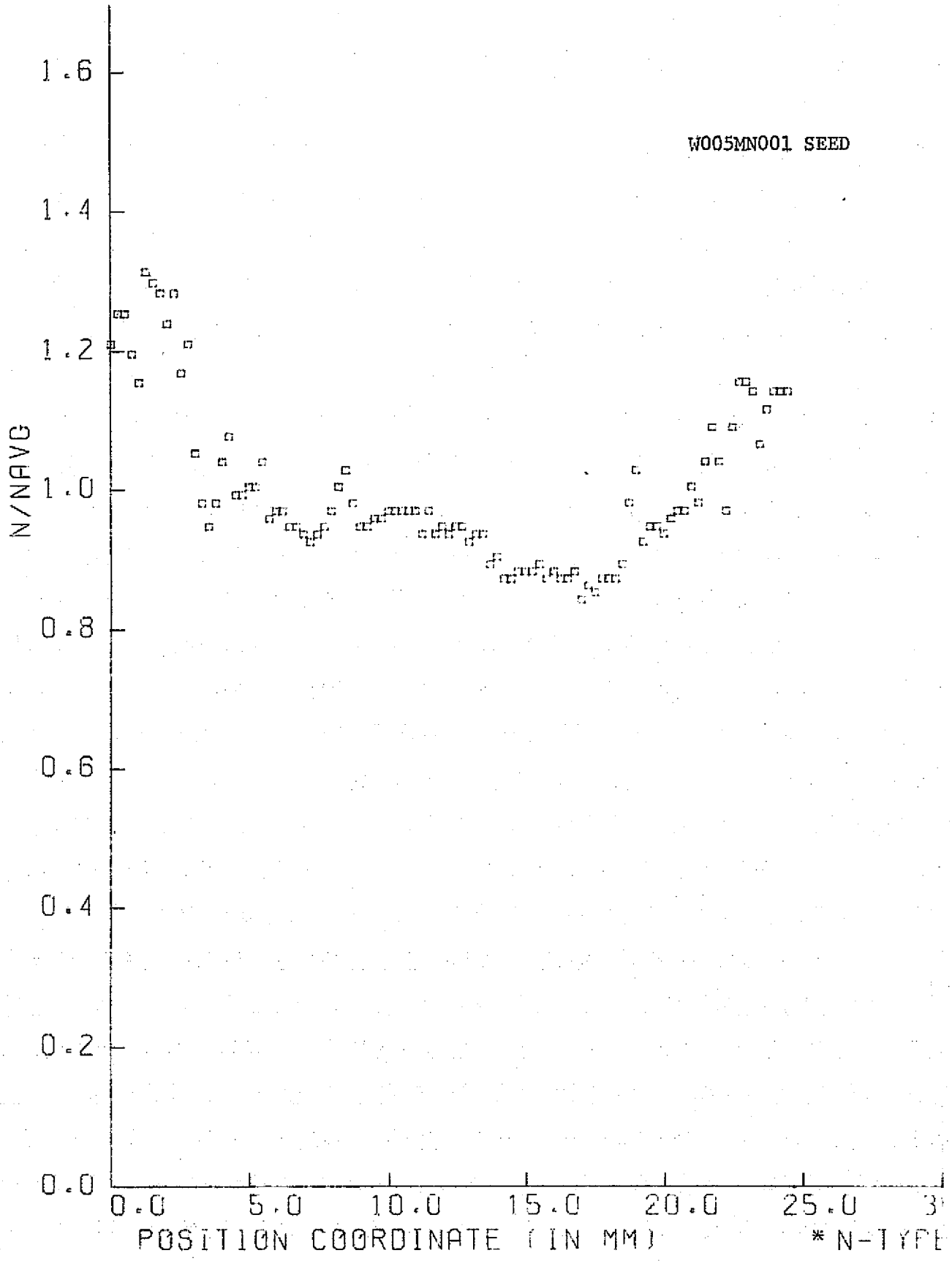

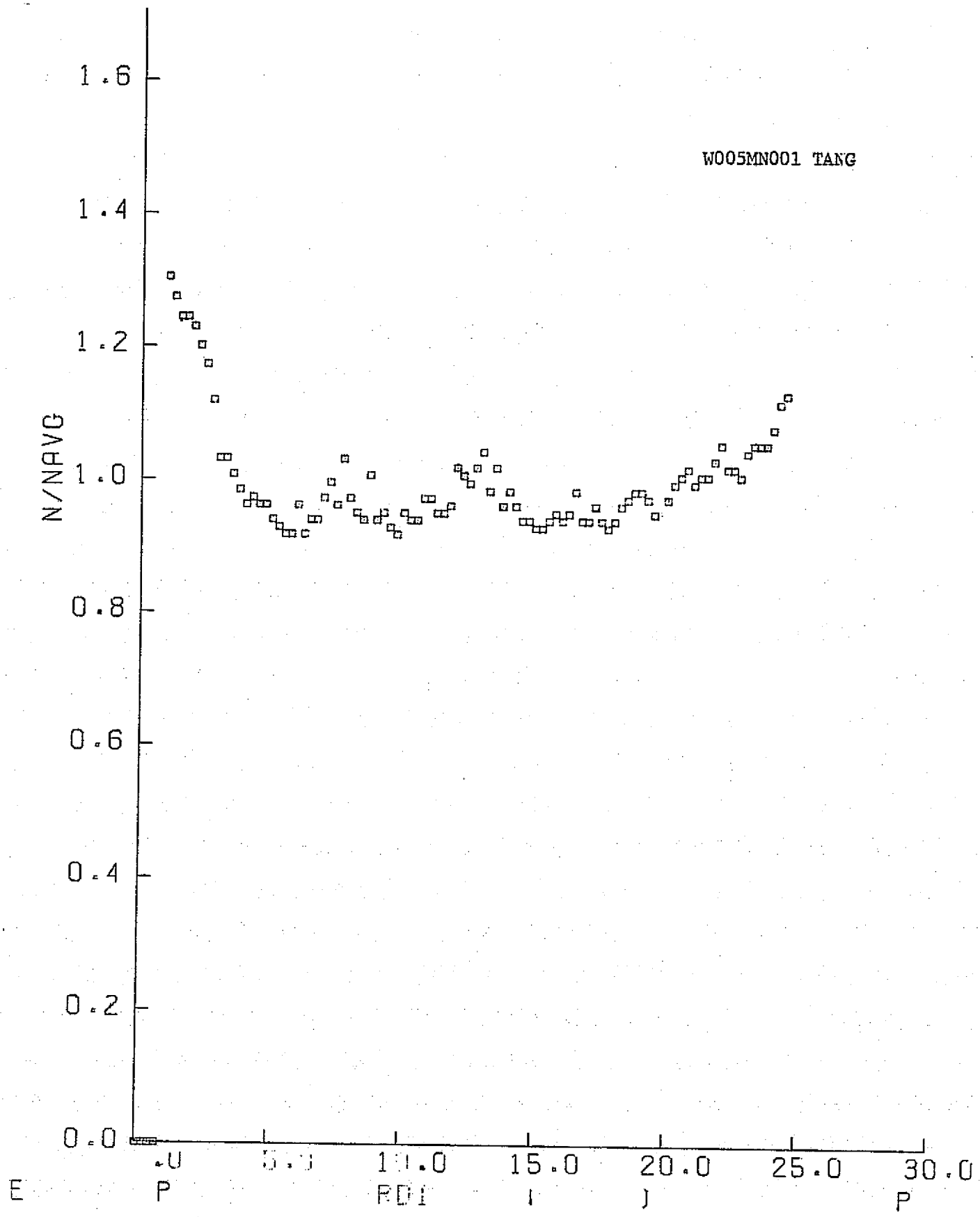

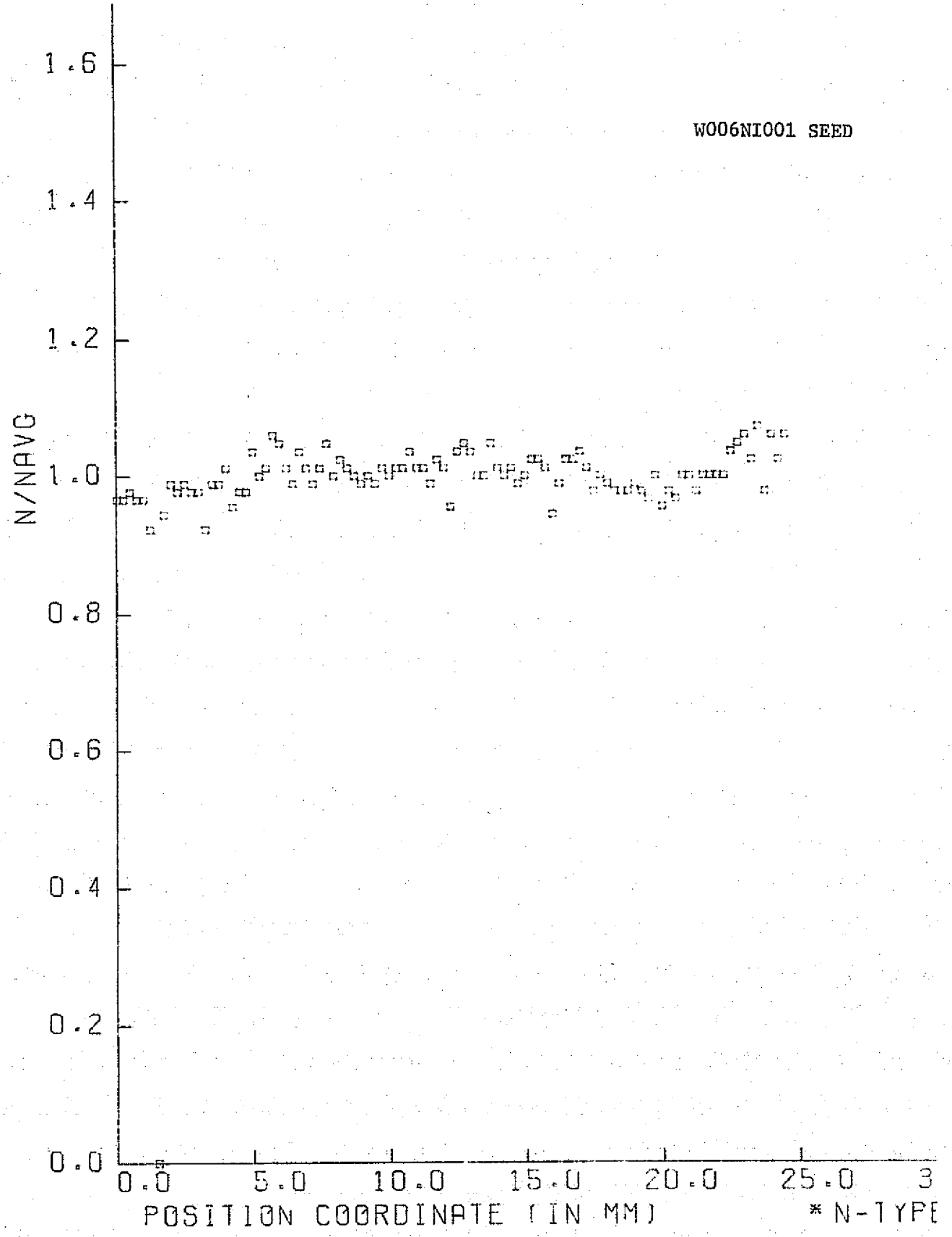

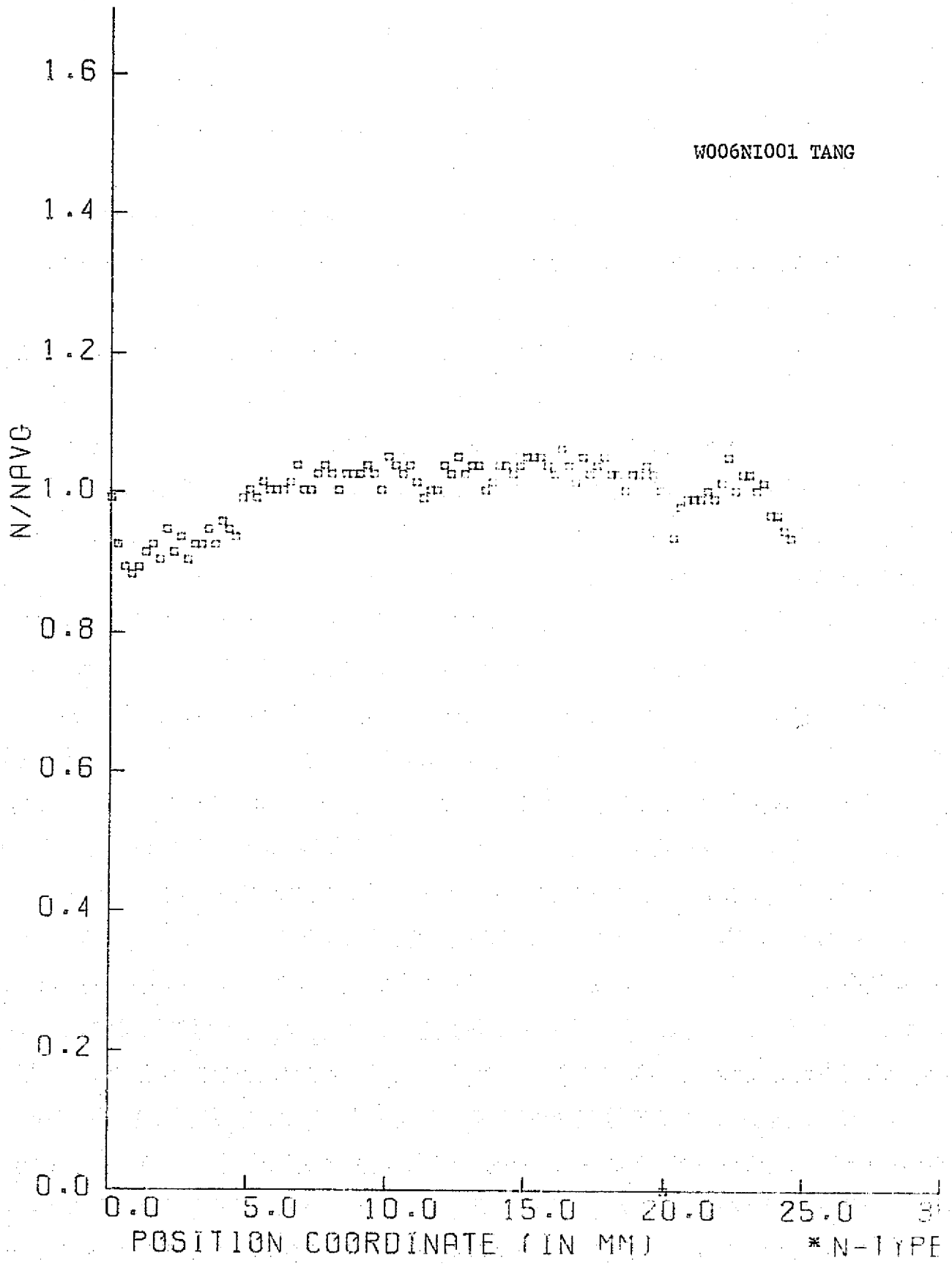

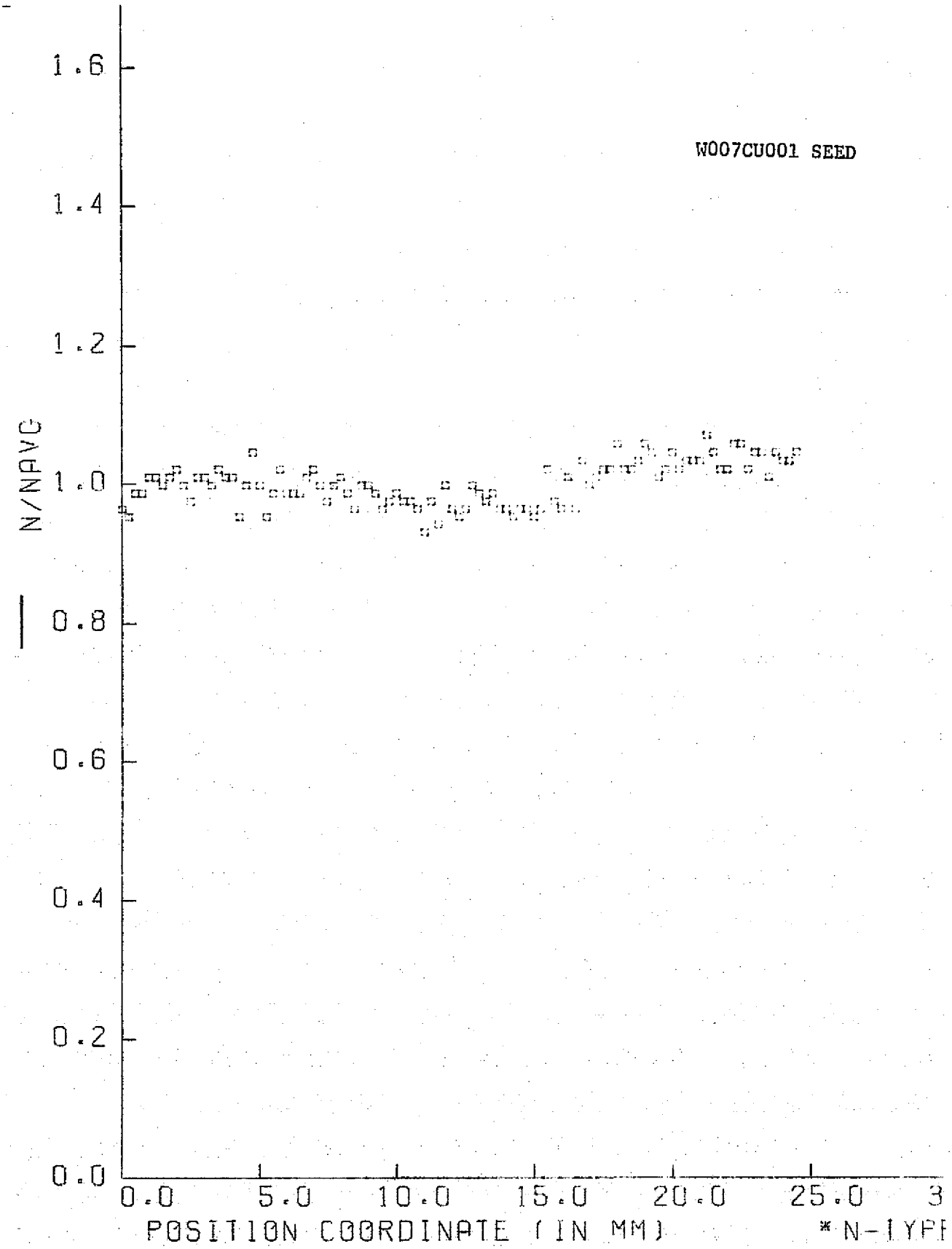

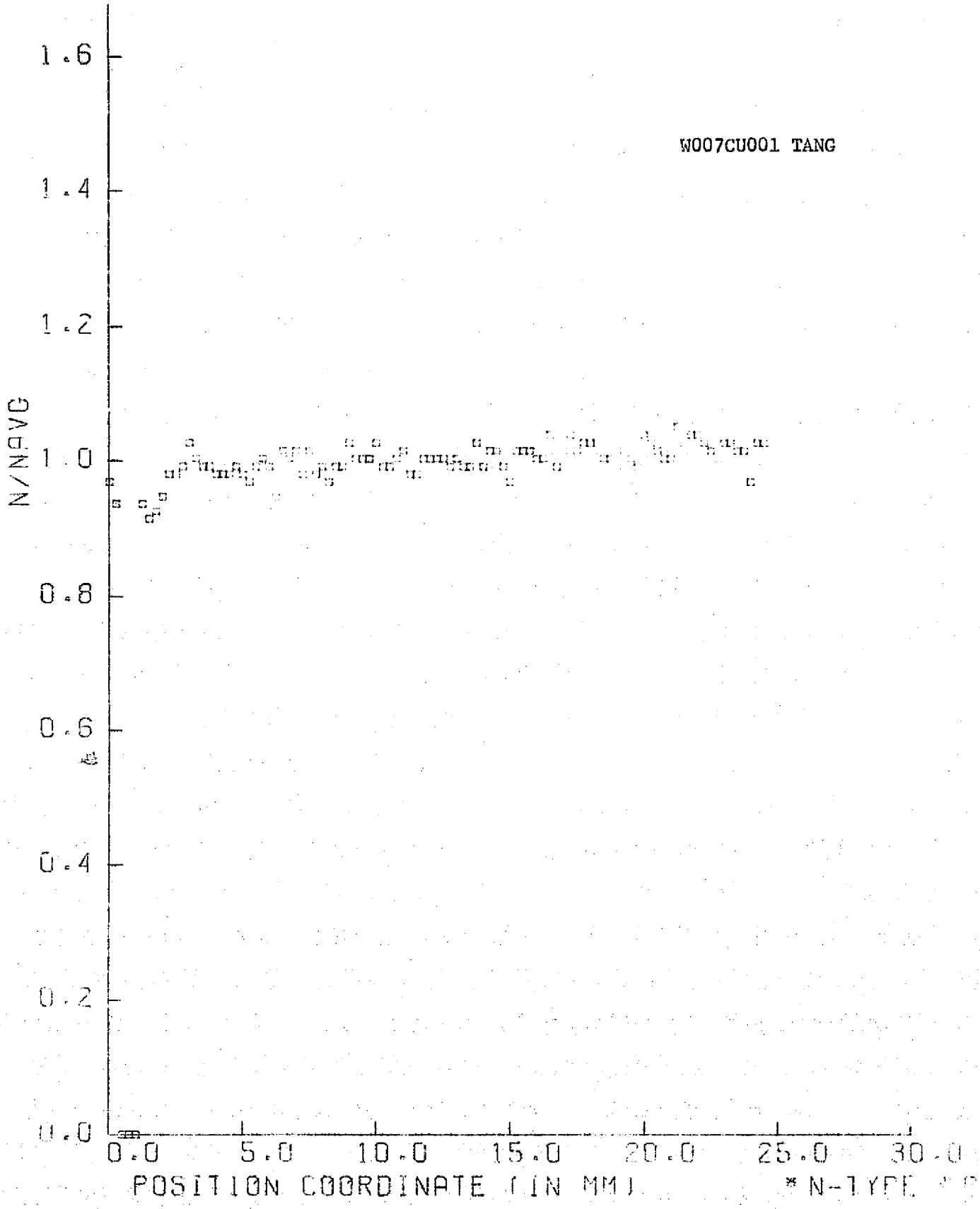

7.2 Appendix 2 — Photovoltaic Characteristics of Transition Metal Doped Solar Cells under AM1-Equivalent Quartz-Iodine Illumination

- No anti-reflective coatings,
- Cell area = 1 cm^2,
- Illumination 100 mw/cm^2.

Cell run numbers and ingot numbers correspond to those in Table 8, Section 4.3.

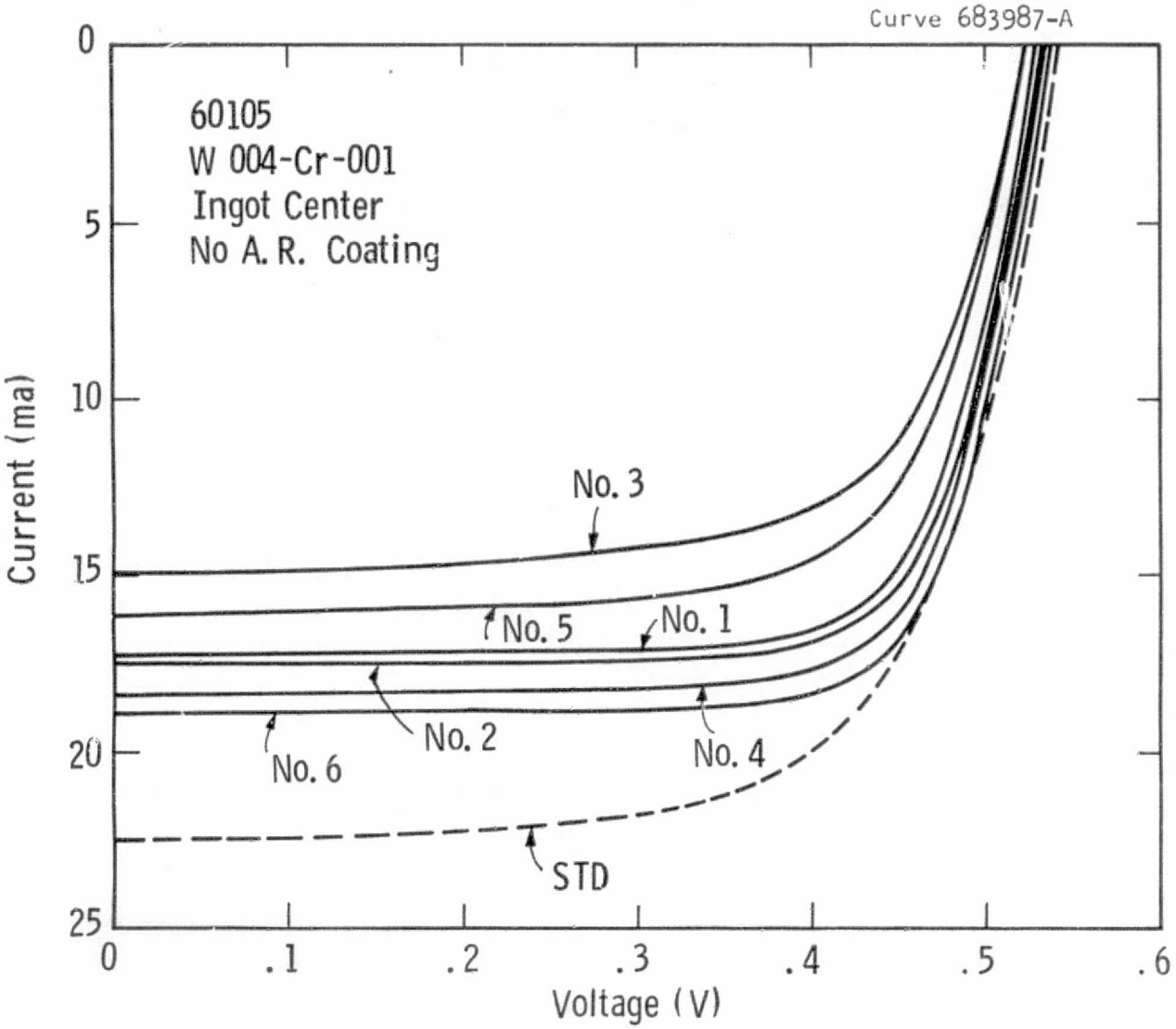
Curve 683987-A
60105
W 004-Cr-001
Ingot Center
No A. R. Coating
No. 3
No. 5
No. 1
No. 2
No. 6
No. 4
STD
Current (ma)
Voltage (V)
0
5
10
15
20
25
0
.1
.2
.3
.4
.5
.6

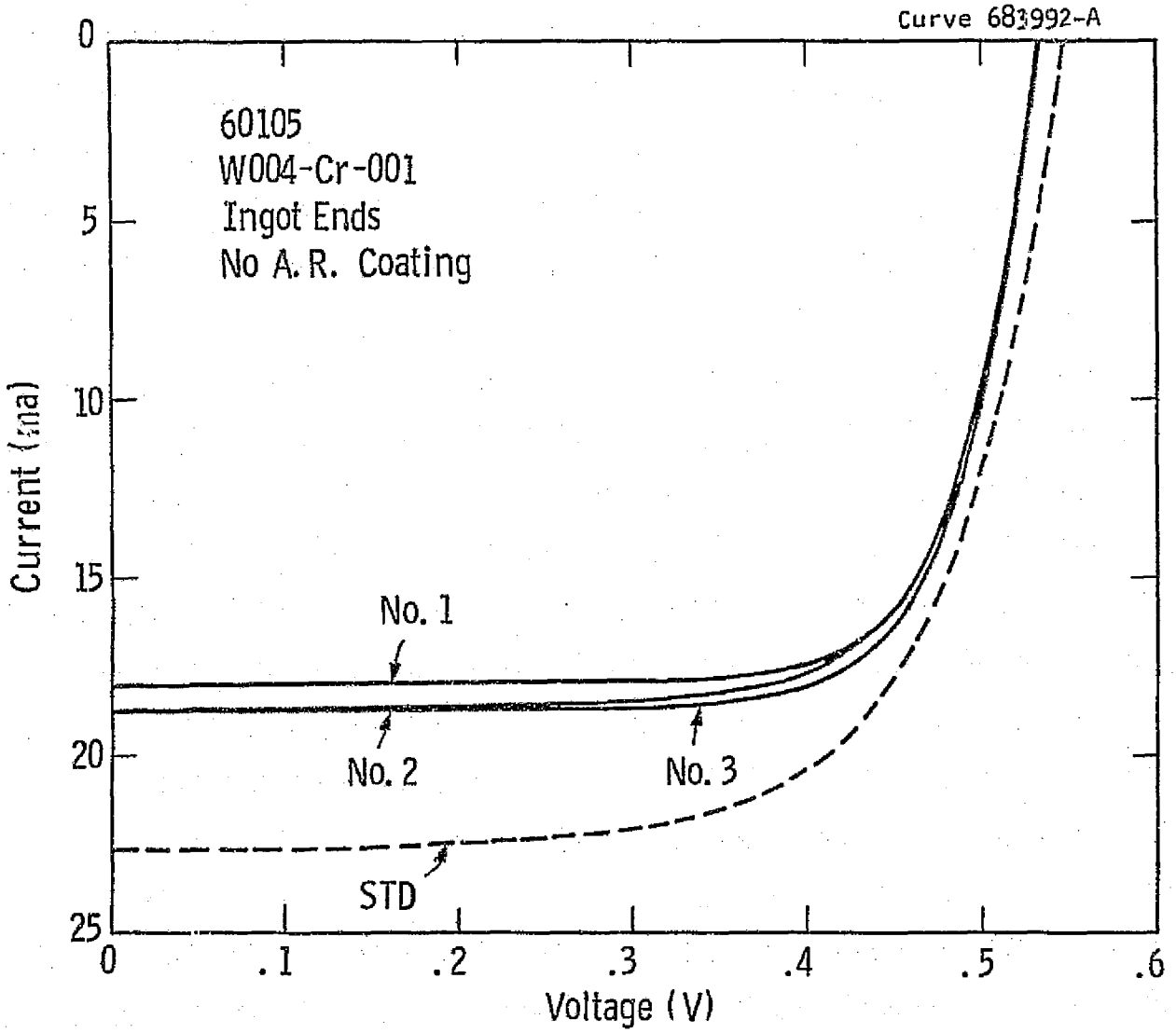
Curve 683992-A
60105
W004-Cr-001
Ingot Ends
No A.R. Coating
No. 1
No. 2
No. 3
STD
Current (ma)
Voltage (V)
0
5
10
15
20
25
0
.1
.2
.3
.4
.5
.6

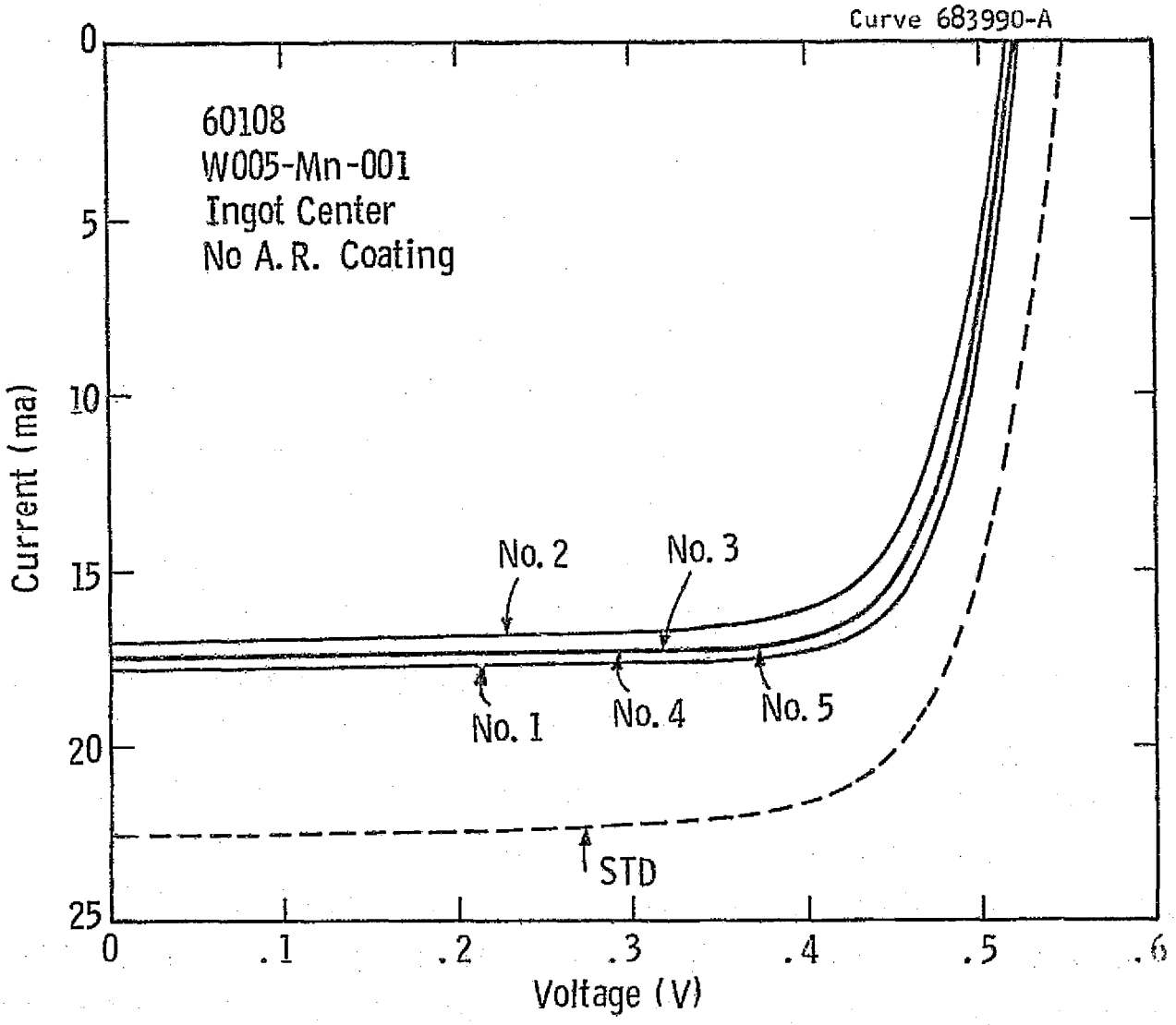
Curve 683990-A
60108
W005-Mn-001
Ingot Center
No A.R. Coating
No. 1
No. 2
No. 3
No. 4
No. 5
STD
Current (ma)
Voltage (V)
0
5
10
15
20
25
0
.1
.2
.3
.4
.5
.6

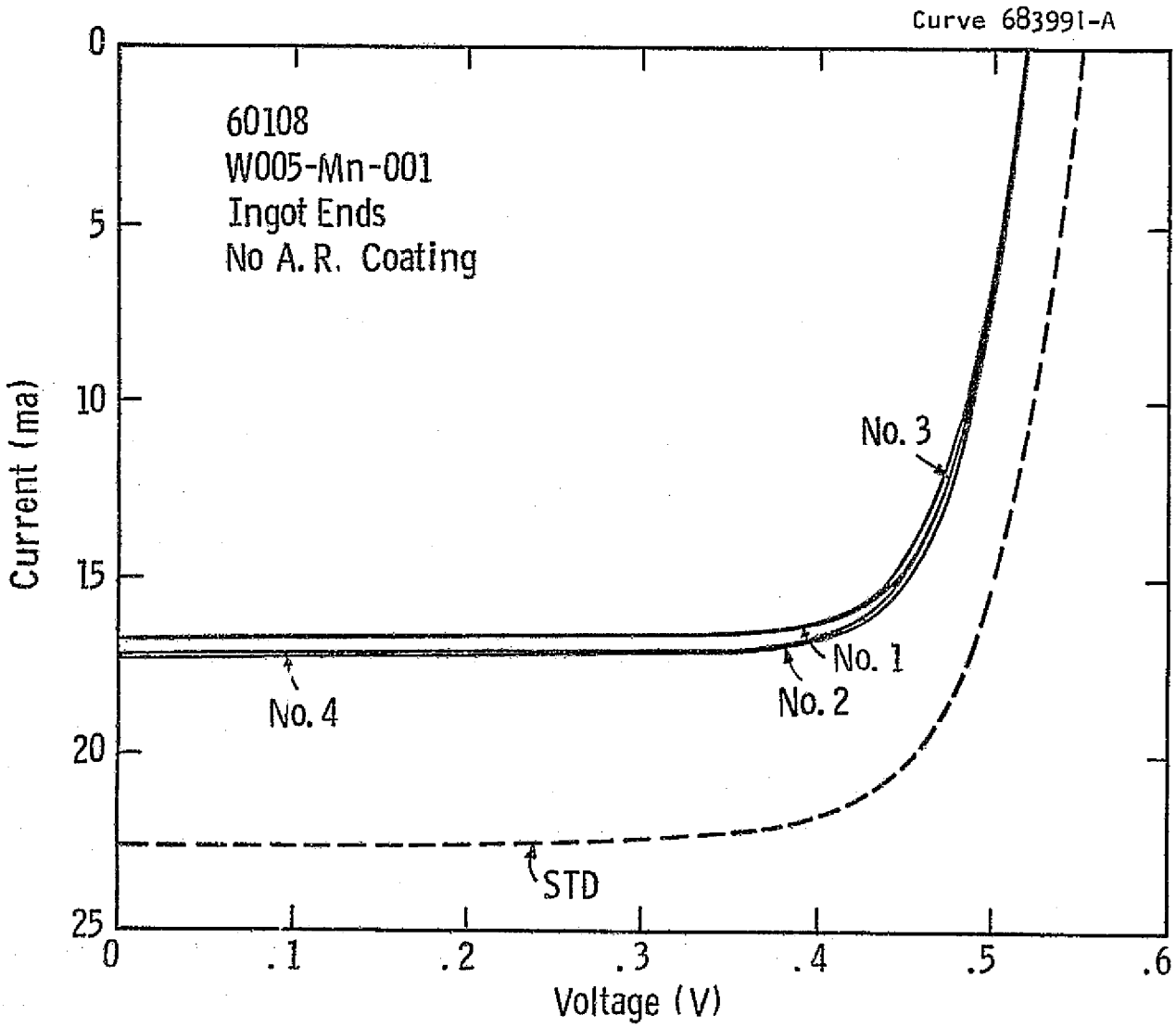
Curve 683991-A
60108
W005-Mn-001
Ingot Ends
No A. R. Coating
No. 3
No. 1
No. 2
No. 4
STD
Current (ma)
Voltage (V)
0
5
10
15
20
25
0
.1
.2
.3
.4
.5
.6

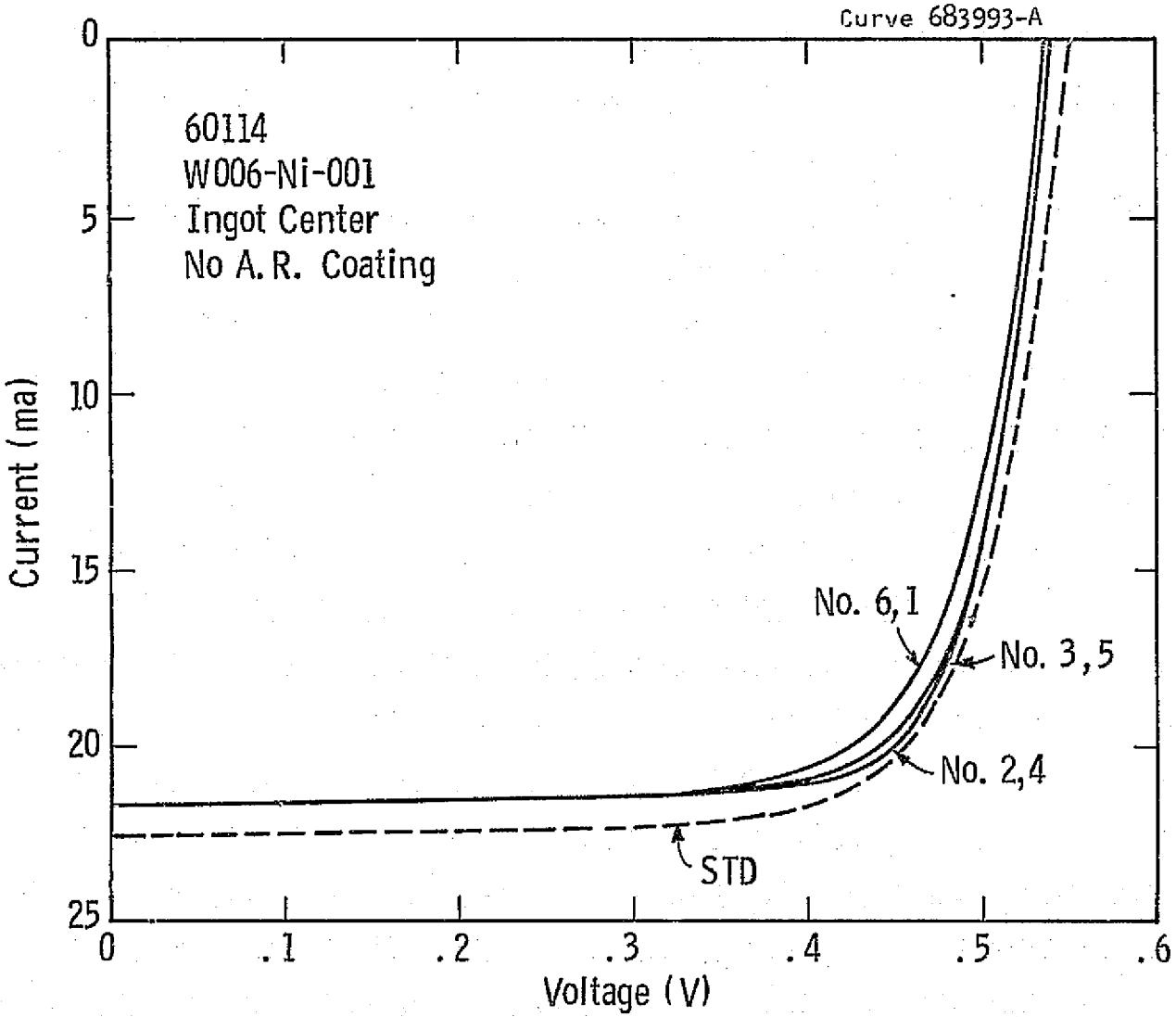
Curve 683993-A
60114
W006-Ni-001
Ingot Center
No A.R. Coating
No. 6,1
No. 3,5
No. 2,4
STD
Current (ma)
Voltage (V)
0
5
10
15
20
25
0
.1
.2
.3
.4
.5
.6

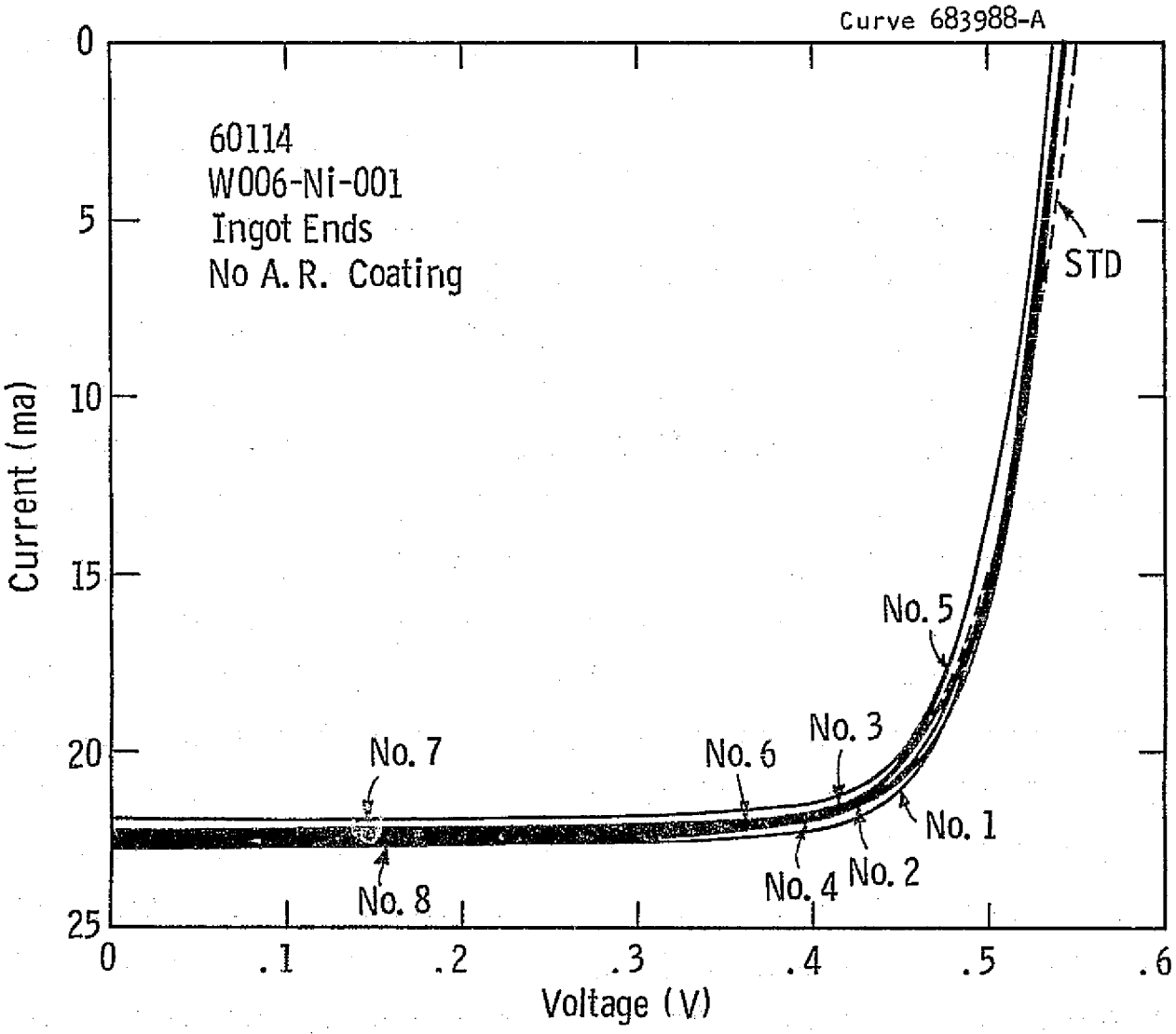
Curve 683988-A
60114
W006-Ni-001
Ingot Ends
No A.R. Coating
STD
No. 5
No. 3
No. 6
No. 7
No. 1
No. 2
No. 4
No. 8
Current (ma)
Voltage (V)
0
5
10
15
20
25
.1
.2
.3
.4
.5
.6

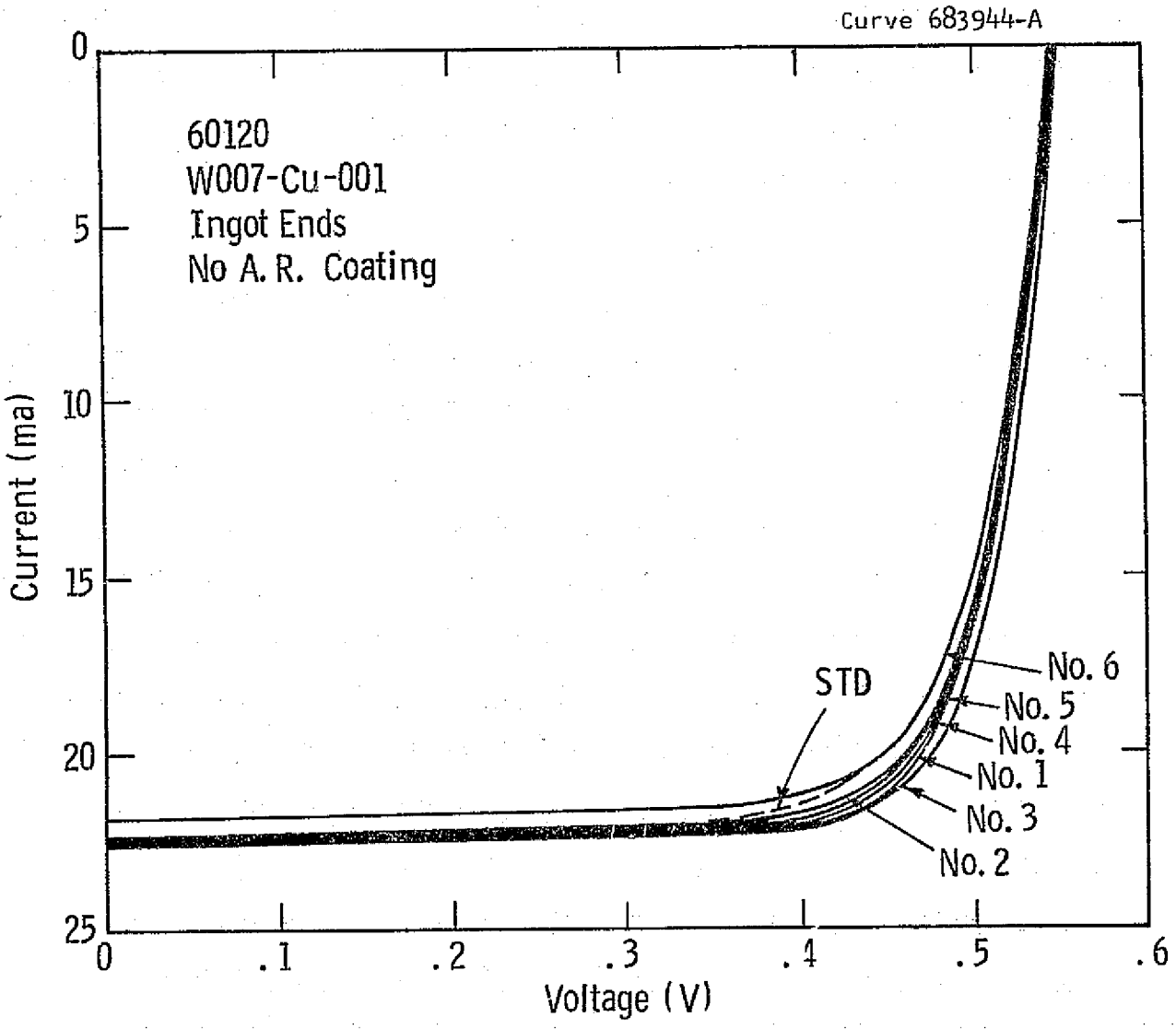
Curve 683944-A
60120
W007-Cu-001
Ingot Ends
No A. R. Coating
STD
No. 6
No. 5
No. 4
No. 1
No. 3
No. 2
Current (ma)
Voltage (V)
0
5
10
15
20
25
0
.1
.2
.3
.4
.5
.6

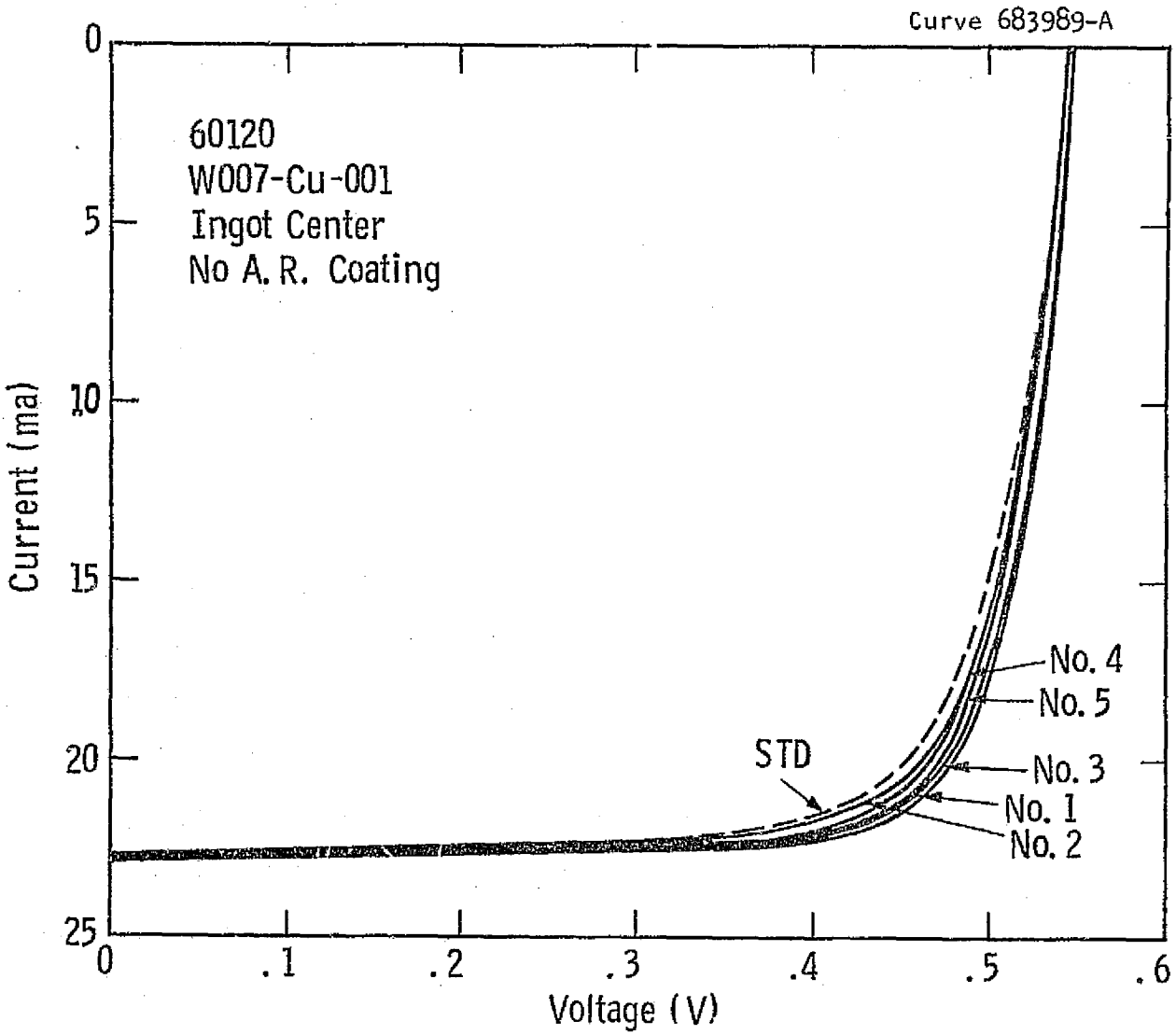
Curve 683989-A
60120
W007-Cu-001
Ingot Center
No A. R. Coating
Current (ma)
0
5
10
15
20
25
0
.1
.2
.3
.4
.5
.6
Voltage (V)
STD
No. 4
No. 5
No. 3
No. 1
No. 2